Hindawi
Geofluids
Volume 2019, Article ID 9502904, 33 pages
https://doi.org/10.1155/2019/9502904

Research Article

Paleo-Hydrothermal Predecessor to Perennial Spring Activity in Thick Permafrost in the Canadian High Arctic, and Its Relation to Deep Salt Structures: Expedition Fiord, Axel Heiberg Island, Nunavut

Marcos Zentilli,[1] **Christopher R. Omelon**,[2] **Jacob Hanley**,[3] **and Darren LeFort**[3]

[1]*Department of Earth Sciences, Dalhousie University, Halifax, Nova Scotia, Canada*
[2]*Department of Geology, University of Kansas, Lawrence, Kansas, USA*
[3]*Department of Geology, Saint Mary's University, Halifax, Nova Scotia, Canada*

Correspondence should be addressed to Marcos Zentilli; zentilli@dal.ca

Received 8 June 2018; Accepted 10 October 2018; Published 2 June 2019

Academic Editor: Domenico Montanari

It is surprising to encounter active saline spring activity at a constant 6°C temperature year-round not far away from the North Pole, at latitude 79°24′N, where the permafrost is ca. 600 m thick and average annual temperature is -15°C. These perennial springs in Expedition Fiord, Queen Elizabeth Islands, Canadian Arctic Archipelago, had previously been explained as a recent, periglacial process. However, the discovery near White Glacier (79°26.66′N; 90°42.20′W; 350 m.a.s.l.) of a network of veins of hydrothermal origin with a similar mineralogy to travertine precipitates formed by the springs suggests that their fluids have much deeper circulation and are related to evaporite structures (salt diapirs) that underlie the area. The relatively high minimum trapping temperature of the fluid inclusions (avg. ~200 ± 45°C, 1σ) in carbonate and quartz in the vein array, and in quartz veins west of the site, explains a local thermal anomaly detected through low-temperature thermochronology. This paper reviews and updates descriptive features of the perennial springs in Expedition Fiord and compares their mineralogy, geochemistry, and geology to the vein array by White Glacier, which is interpreted as a hydrothermal predecessor of the springs. The perennial springs in Axel Heiberg Island are known for half a century and have been extensively described in the literature. Discharging spring waters are hypersaline (1-4 molal NaCl; ~5 to 19 wt% NaCl) and precipitate Fe-sulfides, sulfates, carbonates, and halides with acicular and banded textures representing discharge pulsations. At several sites, waters and sediments by spring outlets host microbial communities that are supported by carbon- and energy-rich reduced substrates including sulfur and methane. They have been studied as possible analogs for life-supporting environments in Mars. The vein array at White Glacier consists of steep to subhorizontal veins, mineralized fractures, and breccias within a gossan area of ca. 350 × 50 m. The host rock is altered diabase and a chaotic matrix-supported breccia composed of limestone, sandstone, and anhydrite-gypsum. Mineralization consists of brown calcite (pseudomorph after aragonite) in radial aggregates as linings of fractures and cavities, with transparent, sparry calcite and quartz at the centre of larger cavities. Abundant sulfides pyrite and marcasite and minor chalcopyrite, sphalerite, and galena occur in masses and veins, much like in base metal deposits known as Mississippi Valley Type; their weathering is responsible for brown Fe oxides forming a gossan. Epidote and chlorite rim veins where the host rock is Fe- and Mg-rich diabase. The banded carbonate textures with organic matter and sulfides are reminiscent of textures observed in mineral precipitates forming in the active springs at Colour Peak Diapir. Very small fluid inclusions (5-10 μm) in two generations of vein calcite (hexagonal, early brown calcite we denominate "cal1" lining vein walls; white-orange sparry calcite "cal2" infilling veins) have bulk salinities that transition between an early, high-salinity end-member brine (up to ~20 wt% NaCl equivalent) to a later, low-salinity end-member fluid (nearly pure water) and show large fluctuations in salinity with time. Inclusions that occupy secondary planes and also growth zones in the later calcite infilling (deemed primary) have T_h ranging from 100°C to 300°C (n = 120, average~200°C; independent of salinity), 2 orders of magnitude higher than average discharging water temperatures of 6°C at Colour Peak Diapir. Carbon isotope composition ($\delta^{13}C_{VPDB}$) of the White Glacier vein array carbonates ranges from approximately -20 to -30‰, like carbonates formed by the degradation of petroleum, whereas carbonates at Colour Peak Diapir springs have a value of -10‰. Oxygen isotope

composition ($\delta^{18}O_{VSMOW}$) of vein carbonates ranges from -0.3‰ to +3.5‰, compatible with a coeval fluid at 250°C with a composition from -3.5‰ to -7.0‰. These data are consistent with carbonates having precipitated from mixtures of heated formational waters and high-latitude meteoric waters. In contrast, the $\delta^{18}O_{VSMOW}$ value for carbonates at Colour Peak Diapir springs is +10‰, derived from high-latitude meteoric waters at 6°C. The sulfur isotope ($\delta^{34}S_{VCDT}$) composition of Fe-sulfides at the perennial springs is +19.2‰, similar to the $\delta^{34}S_{VCDT}$ of Carboniferous-age sulfate of the diapirs and consistent with low-temperature microbial reduction of finite (closed-system) sulfate. The $\delta^{34}S_{VCDT}$ values of Fe-sulfides in the vein array range from -2.7‰ to +16.4‰, possibly reflecting higher formation temperatures involving reduction of sulfate by organics. We suggest that the similar setting, mineralogical compositions, and textures between the hydrothermal vein array and the active Colour Peak Diapir springs imply a kinship. We suggest that overpressured basinal fluids expelled from the sedimentary package and deforming salt bodies at depth during regional compressional tectonic deformation ca. 50 million years ago (Eocene) during what is known as the Eurekan Orogeny created (by hydrofracturing) the vein array at White Glacier (and probably other similar ones), and the network of conduits created continued to be a pathway around salt bodies for deeply circulating fluids to this day. Fluid inclusion data suggest that the ancient conduit system was at one point too hot to support life but may have been since colonized by microorganisms as the system cooled. Thermochronology data suggest that the hydrologic system cooled to temperatures possibly sustaining life about 10 million years ago, making it since then a viable analogue environment for the establishment of microbial life in similar situations on other planets.

1. Introduction

The presence in a polar region of active saline springs at constant ca. 6°C temperature year-round, where average temperature is -15°C [1] and continuous permafrost is 600 m thick, is astonishing. This is the case in western Axel Heiberg Island (Figure 1), Queen Elizabeth Islands, Canadian Arctic Archipelago, at latitude 79°24′N (e.g. [2–4]). The perennial springs (hereforth PSS) are situated in the periphery of evaporite diapirs (bodies of salt, anhydrite, and gypsum) that underlie the Expedition Fiord area (Figures 2 and 3(a)) and have risen over time as a ductile solid from their ultimate source in beds at ca. 10 km depth in the Sverdrup sedimentary basin (Figure 1; e.g., [5, 6]). The springs have been attributed to Quaternary periglacial processes (e.g., [7]). However, during a regional study of the uplift and thermal history of the archipelago using apatite fission-track thermochronology [8–10], it was noticed that the area where the PSS occur at the head of Expedition Fiord cooled to ca. 100°C between 20 and 30 million years later than the rest of the region (Figure 4). This realization led to a search for evidence for the pervasive circulation of warm fluids in the area in the form of veins with minerals amenable to fluid inclusion studies. In 2006, a network or array of mineral veins of hydrothermal origin was identified adjacent to White Glacier (Figures 2 and 3(b)). The White Glacier vein array (hereforth WGVA) is accompanied by a colourful gossan arising from the weathering of base metal (Fe, Cu, Zn, and Pb) sulfides and is the subject of this paper. We first update the descriptive features of the local PSS and then compare the WGVA with the prominent Colour Peak Diapir, ~13.7 km distant (Figures 2 and 3(a)), and two other PSS at Expedition Diapir and Wolf Diapir in terms of mineralogy, fluid inclusion systematics, and geochemistry, including stable O, C, and S isotope compositions. Based on the above studies and the literature, we conclude that the PSS have a kinship with the WGVA and the latter owes its existence to focussed expulsion of overpressured, hot, basinal fluids from an evaporite-dominated basement during tectonic compression known as the Eurekan Orogeny predominantly during the Eocene [11, 12]. The WGVA thus may represent the establishment of a plumbing system that has been later exploited by the PSS. The WGVA also is evidence for a regional metallogenic process that may have formed mineral concentrations elsewhere.

Permafrost at high latitudes is traditionally considered to effectively separate groundwater flow systems into two zones: a shallow, supra-permafrost zone that is active during summer months when air temperatures exceed 0°C and a sub-permafrost region that is hydrologically disconnected from the Earth's surface [13]. The impervious nature of continuous permafrost means that such systems are poorly understood [14]; having a window into the subsurface through groundwater spring activity, therefore, provides a rare opportunity to further our understanding of hydrologic activity in polar environments, to explore life beneath permafrost, and to improve our appreciation of the potential for bioavailable water and subsurface life to exist on other planets such as Mars [15–18]. The update of data on these anomalous polar springs and new interpretation of their process is a contribution to the understanding of geothermal systems in salt-dominated terrains.

2. Geological Setting

The perennial springs and WGVA lie within a relatively small area of the extensive (1000 km by 350 km) Sverdrup Basin (Figure 1), which contains a thickness of over 13 km of sedimentary and volcanic rocks ranging in age from Carboniferous to Tertiary [19]. The basin has been extensively explored for petroleum [20], although the wells in the eastern Sverdrup Basin have been disappointing and are more likely to produce gas than oil, due to the intervention of tectonism and the thermal effects of igneous intrusions [21]. The geology of the Expedition Fiord area (Figure 2) was initially mapped during the Jacobsen-McGill Arctic Research Expedition (1959-1962), among others by Tozer [22], Thorsteinsson and Tozer [23], and Fricker [24]. The evaporite diapirs were described by Hoen [25, 26]. A new map of the area including both Expedition Fiord and Strand Fiord was produced by Harrison and Jackson [27] and salt-induced structures reinterpreted by Jackson and Harrison [6]; their latter paper provides a valuable geological introduction to this study. The oldest rock unit exposed in the

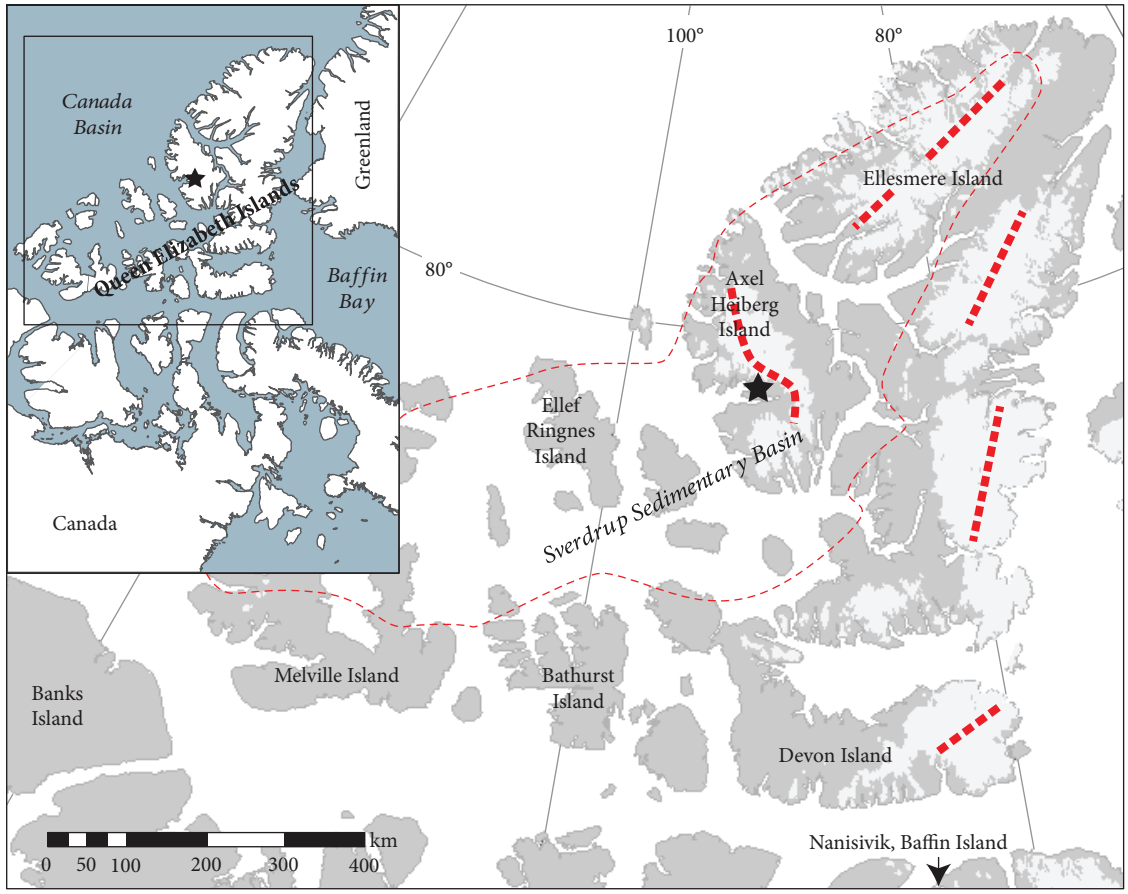

Figure 1: Location map of the White Glacier site (star) in Axel Heiberg Island, Queen Elizabeth Islands, Canadian Arctic Archipelago. Icefields are light grey, generally capping 1500–2000 m high mountains (dotted lines). The dashed line outlines the Sverdrup Basin with a thickness of up to 12 km of Paleozoic to Paleogene sedimentary and volcanic rocks, including Carboniferous salt beds at depth and diapiric salt-anhydrite-gypsum structures that reach the surface.

immediate area is allochthonous gypsum and anhydrite of the Otto Fiord Fm. of Lower Carboniferous age (in red in Figure 2), contained in diapiric bodies [5]. Ductile salt and evaporites rose and intruded the thick (12-15 km) sedimentary succession of the Sverdrup Basin [5]. The oldest exposed stratified rocks are Upper Permian to Middle Jurassic marine sandstones and shales, overlain by Jurassic to Cretaceous sandstones and limestones. The Mesozoic succession contains extensive volcanic units of basalt and sets of intrusive sills and dikes of diabase (intrusive basalt) of middle Cretaceous age (^{40}Ar-^{39}Ar dates from 129 to 80 Ma; [28]). The evaporite diapirs also contain rafts of diabase (Figure 2). Further afield are Cenozoic sediments of Paleocene to Eocene age, some disrupted by the mechanically intrusive evaporite diapirs, which may be actively rising [29]. Quaternary deposits consist of glacial and fluvial gravels and sands.

2.1. Eurekan Orogeny. The Paleozoic to Paleocene strata of the Sverdrup Basin were folded during the Paleogene Eurekan Orogeny into irregular synclines and anticlines with wavelengths of ca. 5 to 10 km. Distorted ramparts of diapiric anhydrite crop out in the cores of tight anticlines, and wider synclinal basins separate the diapiric walls. The most prominent faults are N-S, east-verging thrust faults that are interpreted by Jackson and Harrison [6] to be rooted in an evaporite canopy (extruded subhorizontal salt-anhydrite sheet) at depth. Important is a thrust fault south of Thompson Glacier at the head of Expedition River (rightmost side of Figure 2), which places Upper Permian rocks (Blind Fiord Fm.) and Carboniferous evaporite over Jurassic and Cretaceous strata. In addition, there are intermediate faults north of Expedition Diapir and Colour Peak Diapir, and the WGVA site is located at the intersection of a major WNW fault and a diabase intrusion of Cretaceous age (Figure 2). Minor faults and shattered zones (not indicated in Figure 2) abound around the evaporite diapirs, especially where ductility contrasts exist, such as between mafic igneous rocks and sedimentary rocks.

2.2. Wall and Basin Structure. Evaporite diapirs are conspicuous features in the Expedition Fiord area [25, 26]; they are clustered and irregular in shape, some forming walls and slivers [27]. Three clusters are identified in the local area from west to east: Colour Peak Diapir, Expedition Diapir (Gypsum Hill – Little Matterhorn Diapir), and a sliver east of Thompson Glacier (Figure 2). Early workers called the complexly folded region intermixed with encroaching diapirs a "wall-and-basin structure" (WABS; [30]). Schwerdtner and

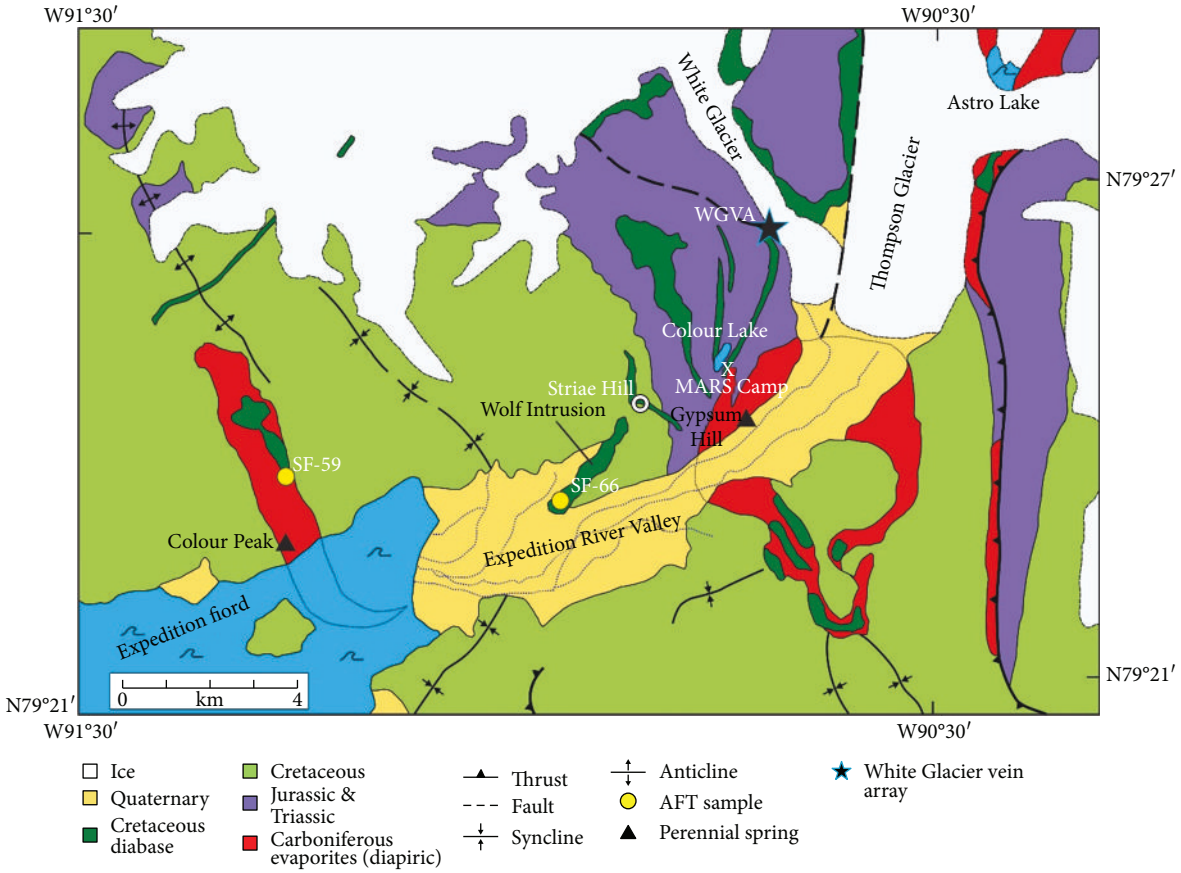

Figure 2: Generalized geological map showing the location of the White Glacier vein array site (black star) in relation to perennial springs (black triangles) and evaporite diapirs (red); purple and light green units are predominantly sedimentary strata of Mesozoic age; igneous mafic sills and dikes are dark green. Location of apatite fission track samples in Wolf Intrusion and Colour Peak marked as filled yellow circles. Fluid inclusion Striae Hill sample marked by white ring. MARS Camp (McGill Arctic Research Station - X) was used as field base. Geology modified from Harrison and Jackson [27].

Van Kranendonk [31] described this feature as "crooked walls of diapiric anhydrite contained in folded clastic rocks." The diapirs occupy the cores of narrow polygonal to oval anticlines. Jackson and Harrison [6] proposed that this restricted WABS province resulted from the development of a coalescing layer or canopy of evaporite rocks during the early Cretaceous; these evaporitic rocks would have plastically spread laterally and formed at depth the roots of now-exposed secondary diapirs created during compression, thrusting, and folding in the Paleogene (mainly Eocene) Eurekan Orogeny.

2.3. Diapirs and Springs. At the surface, the diapirs are composed of anhydrite with a carapace of porous gypsum with blocks of anhydrite, but they are known to have halite at depth from exploration drilling [32] and the presence of exposed halite at Stolz Diapir, located on southeastern Axel Heiberg Island [31]. Despite their susceptibility to erosion and the fact that they disrupt Quaternary deposits, their positive topographic relief (Figure 2) suggests continuing growth, which is being evaluated with satellite interferometry [29]. The position of perennial spring activity adjacent to or within evaporite structures led Nassichuk and Davies [32] to suggest an essential relationship between them.

2.4. Glaciers. The highlands of Expedition Fiord host the Müller Ice Cap, the largest on Axel Heiberg Island, crowning the Princess Margaret Range (2210 m.a.s.l.), ca. 40 km north of the area shown in Figure 2. One of the large outlet glaciers descending from it is the Thompson Glacier (Figure 2), spanning ~34 km in length and ~3 km wide in the ablation area. It dams several lakes, including Astro Lake (upper right corner of Figure 2) and Phantom Lake (2 km east of Astro Lake, outside Figure 2), and meets the White Glacier terminus at 80 m.a.s.l. (cf. [33]). White Glacier is a valley glacier occupying 38.5 km^2, extending from an elevation of 80 m at its present terminus to its source on the mountains to the west at ca. 1782 m.a.s.l.; ice thickness exceeds 400 m in the deepest basins, and the glacier has thinned by approximately 20 m in the vicinity of the WGVA outcrop since 1960 [34]. Glacial activity has resulted in the carving of steep walls into Triassic-Jurassic sedimentary rocks, which in combination with contemporary thinning has exposed the array of hydrothermal veins described here.

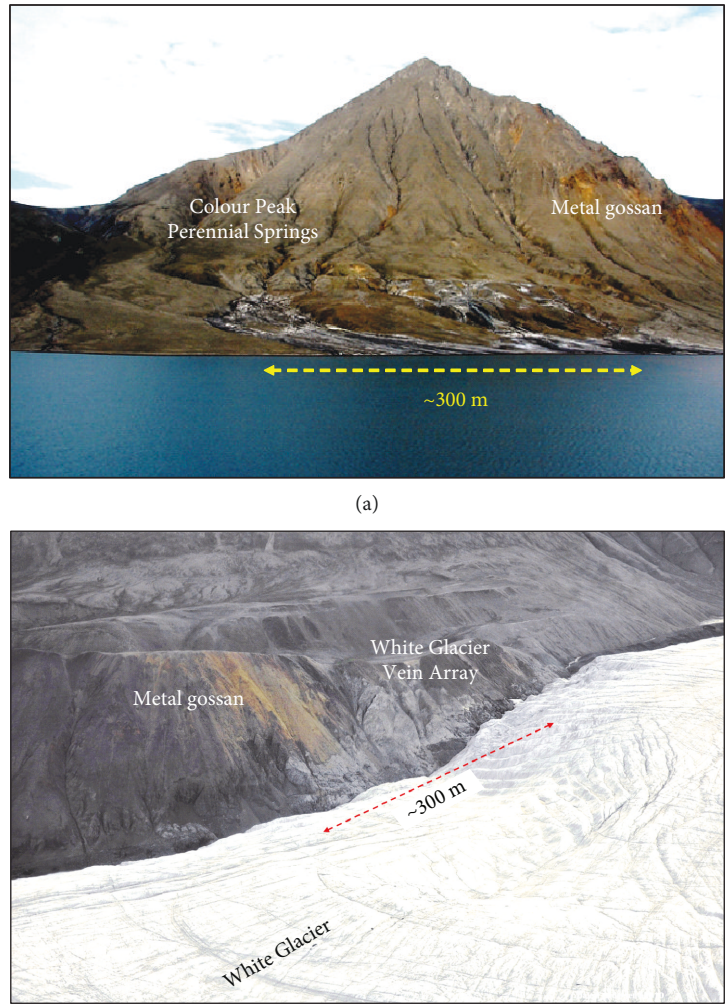

FIGURE 3: (a) Aerial view of travertine deposits at Colour Peak perennial springs (CPS), northern shore of Expedition Fiord, that emit brines at 6°C year-round. The 560 m hill is gypsum and anhydrite, but the colourful gossan denotes weathered iron sulfides associated with rafts of igneous mafic rocks. (b) Aerial view of the whitish vein array (WGVA) on the steep flank of White Glacier, also associated with a gossan (photo by Dale Andersen). Note the similar scale of the two phenomena.

3. Procedures

3.1. Field Work. Foot traverses by M.Z. were undertaken (2006) in the search for any evidence of hydrothermal activity that might help explain the anomalous thermal history results of the area (Table 1). A NE-trending ridge 2 to 3 km NE of the McGill Arctic Research Station (MARS camp, Figure 2), composed of diabase, shows evidence of alteration and gossans derived from oxidation of iron sulfides; the hydrothermal development described here (Figure 3(b)) was found at the intersection of the rusty ridge with White Glacier, which also coincides with the trace of a prominent fault or shear zone (Figure 2). Samples representing the various styles of mineralization were collected (2006, 2009) and prepared as double-polished thin sections (Dalhousie University). Carbonate deposits and fine-grained sediments associated with perennial spring discharge at Colour Peak Diapir (CPS) were collected by C.O. (2011, 2012). Carbonates were prepared as double-polished thin sections (Department of Earth Sciences, Western University); sediments were stored in native spring waters in air-tight serum vials capped with rubber stoppers until analysis.

3.2. Electron Microprobe. Wavelength-dispersive spectroscopic (WDS) electron microprobe analysis (EMP) on WGVA thin sections was completed at the R. MacKay Microprobe Laboratory (Department of Earth Sciences, Dalhousie University) using a JEOL 8200 microprobe operated at an accelerating voltage of 15 kV and a beam current of 20 nA and using a focussed beam (10 s on peak and 10 s off peak counting times; spot size < 1 μm). Qualitative energy-dispersive spectroscopy (EDS) was used initially for confirmation of optical microscopic phase identification.

3.3. X-Ray Fluorescence Mapping. Thin sections from both WGVA and CPS were analyzed by C.O. for trace elements by X-ray fluorescence mapping (μ-XFM) using synchrotron radiation (Advanced Photon Source, Argonne National

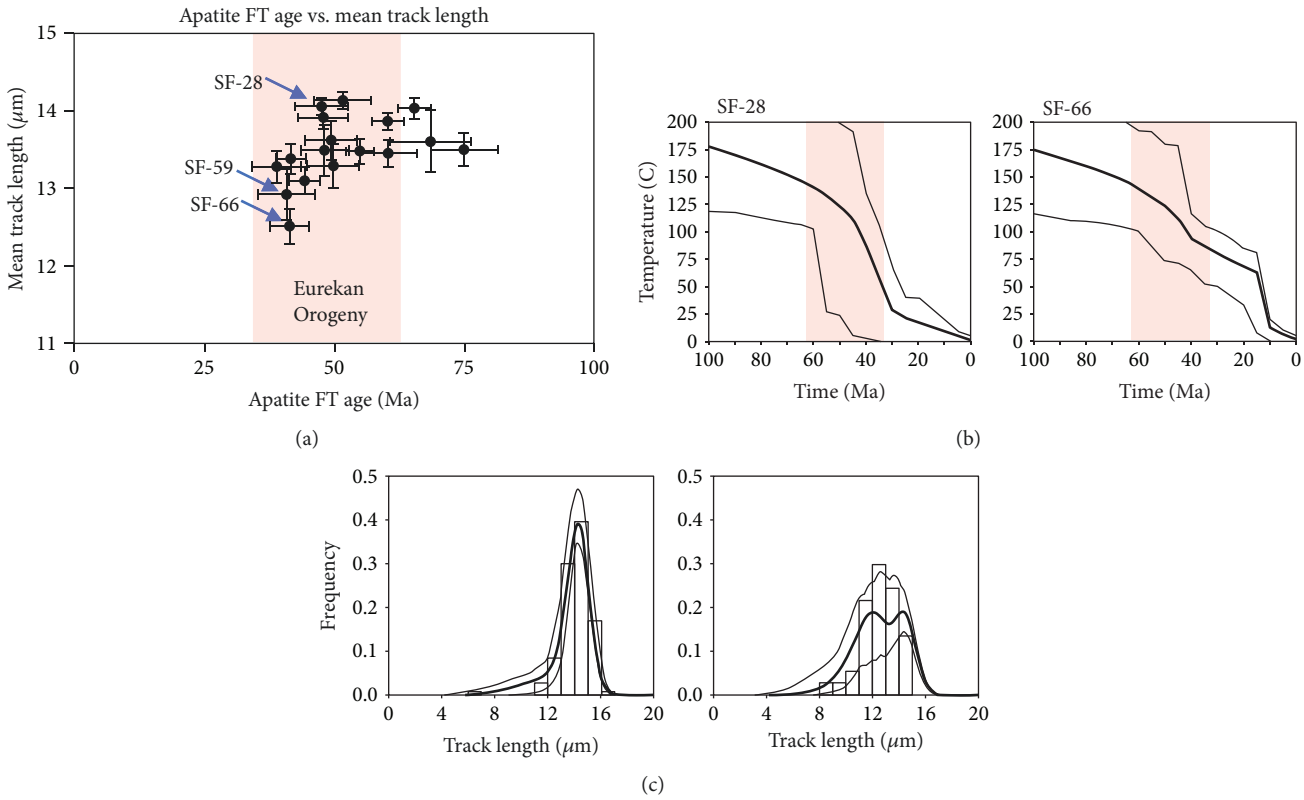

Figure 4: (a) Plot of Apatite Fission Track Age vs. Mean Track Length for samples in the Expedition Fiord area. Note the extreme position in the plot of samples FT-59 and FT-66, from within the area of PSS (see Figure 2). (b, c) Monte Carlo inverse thermal history models for Sverdrup Basin AFT samples using AFTINV [82, 83]. The internally consistent models are compatible with the interpretation that whereas rocks now at the surface in the Princess Margaret Range (60 km to the northeast of Expedition Fiord) cooled rapidly after the Eurekan Orogeny (62 to 33 Ma), rocks in the area of the PSS maintained temperatures of up to 75°C until the Miocene. Note: all models were done using the annealing model of [48]. The middle panels show the upper and lower bounds of time-temperature solution space explored by the 250-300 acceptable model solutions (defined by a K-S goodness of fit statistic) as well as the exponential mean solution, or preferred model (thicker line). The lower panels show the measured length histograms and the exponential mean probability distributions, as well as the upper and lower bounds of the model distributions in the solution set (note that the upper and lower bounds themselves are not solutions). 5 My time steps were used, with new populations of unannealed tracks introduced at 1 My intervals. See text for discussion. Data summary in Table 1.

Laboratory). Incident X-rays passed through a Si 111 monochromator on an insertion device (ID) at 13.5 keV to excite elements up to Pb. The incident beam was focussed to 5 μm × 5 μm using a Kirkpatrick-Baez mirror assembly. Spatially resolved XFM analyses were conducted over specific regions of interest in the samples, which were mounted 45° to the incident beam. The fluorescence X-rays were measured using a 12-element Canberra Ge (Li) detector. The fluorescence X-ray intensity was normalized by the intensity of the incident X-ray beam, and spectral analysis of the fluorescence spectrum of each pixel used to produce two-dimensional maps for each element analyzed.

3.4. Scanning Electron Microscopy. Thin sections and sediments from CPS were analyzed by C.O. by scanning electron microscopy (SEM) at the Western Nanofabrication Facility (Western University) using a LEO (Zeiss) 1540XB FIB/SEM with secondary electron (SE), backscattered electron (BSE), and in-lens detectors. Thin sections were coated with ~5 nm osmium metal, whereas sediments were initially washed in ddH_2O and air-dried before coating with osmium. Samples were imaged at 1-2 keV at a working distance of 4-6 mm. Areas targeted for focussed ion beam (FIB) milling were coarse-milled at 10 nA followed by polishing at 1 nA using Ge at 30 keV. Sediments were also examined by transmission electron microscopy (TEM) at the Biotron (Western University) using a Philips EM 300 TEM. Samples were imaged as wet mounts on carbon-coated Cu grids at 80 keV.

3.5. Confocal Raman Spectroscopy. Confocal laser Raman microspectroscopy (LRM) was used to determine the composition of carbonate minerals, specifically to differentiate between aragonite and calcite polymorphs. LRM analysis was performed by J.H. using a Horiba Jobin-Yvon LabRam HR system at Saint Mary's University. The instrument is equipped with a 100 mW 532 nm Nd-YAG diode laser (Toptica Photonics) and a Synapse charge-coupled device (CCD; Horiba Jobin-Yvon) detector. Pure silicon was used as a frequency calibration standard. Spectra were collected using an 80 μm confocal hole diameter, and a 600-groove/mm grating (spectral resolution of approximately ±2 cm^{-1}). Spectra were

Table 1: Apatite fission track data used for Figure 4.

		Age data								Length data		
Sample number	Grains counted	Rho_s	N_s	Rho_i	N_i	χ^2	Rho_d	N_d	Age ± error (Ma, 1σ)	No. of tracks	Mean ± error (μm, 2σ)	Std. dev. (μm)
ft03-038 SF-16	28	0.168	196	0.423	495	98	1.093	5701	75.0 ± 6.6	49	13.50 ± 0.41	1.43
ft03-041 SF-20	25	0.073	127	0.294	509	100	1.093	5701	47.9 ± 4.8	55	13.91 ± 0.31	1.16
ft03-042 SF-23	25	0.062	126	0.242	489	100	1.093	5701	49.4 ± 5.0	37	13.62 ± 0.49	1.48
ft03-046 SF-27	28	0.101	115	0.379	428	100	1.093	5701	51.6 ± 5.5	57	14.13 ± 0.21	0.79
ft03-047 SF-28	27	0.092	113	0.372	457	81	1.093	5701	47.5 ± 5.2	107	14.05 ± 0.23	1.2
ft03-048 SF-30	25	0.153	159	0.487	505	99	1.093	5701	60.4 ± 5.5	129	13.45 ± 0.33	1.88
ft03-052 SF-36	26	0.911	1299	2.65	3777	1.3	1.093	5701	65.4 ± 3.2	148	14.03 ± 0.25	0.11
ft03-055 SF-41	24	1.101	665	3.5	2114	22	1.093	5701	60.3 ± 3.0	140	13.86 ± 0.22	1.29
ft03-059 SF-47	28	0.712	563	2.49	1967	24	1.093	5701	54.9 ± 2.7	118	13.47 ± 0.32	1.77
ft03-063 SF-51	23	0.167	136	0.667	543	98	1.093	5701	48.1 ± 4.7	25	13.49 ± 0.64	1.54
ft03-067 SF-66	29	0.177	157	0.823	729	39	1.093	5701	41.4 ± 3.8	37	12.51 ± 0.45	1.36
ft04-009 SF-59	28	0.063	67	0.297	315	99	1.093	5701	40.8 ± 5.5	25	12.92 ± 0.65	1.57

A summary of the age and track length data for the Strand Fiord region. Ages reported are the central age [139]. Samples with a chi-square probability greater than 5 pass the chi-square test at the 95% confidence level (i.e., appear to be composed of one age population). N_s, N_i, and N_d are the number of spontaneous, induced, and flux dosimeter (CN-5) tracks, respectively. Rho_s, Rho_i, Rho_d are the density of spontaneous, induced, and dosimeter tracks, respectively ($\times 10^6/cm^2$). A value of 352.5 ± 7.1 (CN-5) was used for the zeta factor. Age error estimates are at the 67% (1σ) confidence level. Mean length error estimates are at the 95% (2σ) confidence level. Alexander M. Grist, Analyst.

collected using an accumulation of three, 50-60-second acquisitions with a laser spot size of ~1-2 micron at 100% laser power (~2.15 mW at sample surface). Spectra from different carbonate types were compared to those in Raman spectral libraries [35].

3.6. Fluid Inclusion Microthermometry. Fluid inclusion microthermometry and imaging was completed by J.H. and D.L. using a Linkham FTIR600 heating-freezing stage mounted on an Olympus BX51 microscope (Department of Geology, Saint Mary's University). Stage calibration was carried out using synthetic fluid inclusion standards containing pure CO_2 (melting at -56.6°C) and pure, critical-density H_2O (melting at 0°C and homogenizing at 374.1°C). Uncertainties for these measurements are ±0.2°C when a heating rate of 1°C/min is used. Final ice melting temperatures were used to calculate salinities [36] and isochoric data were determined using the SOWAT software package [37, 38].

3.7. Stable Isotopes. Pyrite, quartz, and carbonates from vein margins and infillings of the WGVA were sampled using a ~0.5 mm tungsten carbide drill bit to produce powders. These powders were analyzed at Queen's University Facility for Isotope Research (QFIR; Kingston, Ontario). Carbonates were reacted on a gas bench coupled to a Thermo Finnigan Delta Plus XP Isotope Ratio Mass Spectrometer (also using continuous flow). Oxygen from quartz was extracted using a conventional bromine pentafluoride extraction line, with the isotopes measured on a Finnigan Mat 252 Isotope Ratio Mass Spectrometer. Analytical uncertainties on the analyses are ±0.3‰ for O in silicates and ±0.2‰ for C and O in carbonates (K. Klassen, personal communication). Values are reported in the δ notation in units of per mil (‰) relative to Pee Dee Belemnite (VPDB) and Vienna Standard Mean Ocean Water (VSMOW), respectively. Stable sulfur isotope measurements were obtained using a Carlo Erba NCS 2500 elemental analyzer coupled to a Finnigan MAT 252 mass spectrometer with a Finnigan MAT Conflo 11. One sample of pyrite from the Colour Peak perennial springs was also analyzed. Values are reported in the δ notation in units of per mil (‰) relative to standard Vienna Canyon Diablo Troilite (VCDT). Replicate $\delta^{34}S_{VCDT}$ analyses are reproducible to within ±0.3‰ (K. Klassen, personal communication).

3.8. Trace Elements. Trace elements in carbonates were determined by J.H. using laser ablation inductively coupled plasma mass spectrometry (LA-ICP-MS) at the Swiss Federal Institute of Technology (ETH Zurich). Aerosols were generated using a GEOLAS (now Coherent Inc.) 193 nm ArF excimer laser [39]. Aerosols were generated using a pulsed (10 Hz) laser beam with an energy-homogenized beam profile at a fluence of 15 J·cm^{-2} (80-90 mJ output energy) [40]. An Ar-He gas mixture (He 1.15 L/min; Ar 0.8 L/min) carried sample aerosols into an ELAN 6100 quadrupole ICP-MS using similar conditions as Pettke et al. [41]. Oxide production rates were maintained below 0.3%. Mass spectrometer dwell time was set to 10 ms for all masses measured. Quantification of trace element concentrations was performed using the software SILLS [42]. The standard reference glass 610 from NIST was used to calibrate analyte sensitivities. Stoichiometric Ca (40 wt %) was used as the internal standard value as carbonates were determined to be ~$CaCO_3$ with minor impurities (<0.4 wt % total Fe + Mg + Mn).

Table 2: Summary data of the major geochemical parameters of waters collected from spring outflows (Gypsum Hill Springs, Colour Peak Springs, and Wolf Springs) and associated hydrologic measurements. Given that numerous spring outlets exist at Expedition Diapir and Colour Peak Diapir, geochemical data shown here represent the average of previously reported results. Concentrations of cations and anions are expressed in mol/kg. *Q* at Expedition Diapir and Colour Peak represent the sum of all outlets, whereas only one outlet exists at Wolf Diapir. N.D. = not determined. Data collected since 1997 (C.R. Omelon, MSc thesis); Pollard et al. [3]; Omelon et al. [55, 56]; Perrault et al. [64]; Niederberger et al. [63], Lay et al. [60]; Battler et al. [57].

	Expedition Diapir (GHS)	Colour Peak Diapir (CPS)	Wolf Diapir (WS)
Q (L/s)	10-15	20–25	4-5
T (°C)	6.3	6.1	-2.0
pH	7.4	6.1	5.8
ORP (mV)	-283	-312	-171
DO (%)	0.4	0.2	0.5
Salinity (%)	8	16	24
Na^+	1.15	2.01	3.28
Ca^{2+}	0.05	0.08	0.03
Mg^{2+}	0.004	0.011	0.012
K^+	0.002	0.005	0.004
Fe^{2+}	3.1×10^{-6}	1.4×10^{-5}	1.1×10^{-5}
NH_4^+	5.7×10^{-5}	2.2×10^{-4}	5.5×10^{-5}
Cl^-	1.11	2.02	3.05
SO_4^{2-}	0.09	0.08	0.11
NO_3^-	0.0014	0.0002	0.0004
HCO_3^-	0.0009	0.003	0.0005
HS^-	0.0006	6.9×10^{-5}	1.7×10^{-5}

3.9. Fission Track Thermochronology. The fission-track low-temperature thermochronological method as applied in this study at Dalhousie University has been fully explained in Grist and Zentilli [43] and references therein. It is based on the measured density and length distribution of linear tracks of crystal damage produced during spontaneous fission of trace amounts of ^{238}U. In monotonically cooling systems, track densities provide a measure of age with respect to the closure temperature, which for apatite (a U-bearing calcium phosphate) is ca. 100°C over geologically meaningful time periods on the order of 10-100 Ma. Assuming a geothermal gradient of 30°C/km, this corresponds to a burial depth of 4-5 km. It is this temperature-dependent behaviour between 60°C and ~130°C (the partial-annealing zone or PAZ) that allows the apatite FT method to be used as a low-temperature thermochronometer. Reviews of the method, its application to geological problems, and the development of FT thermal models have been provided by Wagner and Van den Haute

[44], Ravenhurst and Donelick [45], Gallagher et al. [46], and Gleadow and Brown [47]. All models were done using the Laslett et al. [48] annealing model; for the modelling, the accepted initial reduction in mean length to 15 μm was introduced (i.e., [49]). Data are shown in Figure 4 and Table 1.

4. Review of the Perennial Springs (PSS)

Examples of perennial groundwater discharge in the Canadian high Arctic have been documented at eight locations on Axel Heiberg Island [50, 51] and two on Ellesmere Island [52, 53]. While those on Ellesmere Island are linked to subglacial hydrology and geologic faults, saline perennial discharge having received the most attention occurs marginal to or near large evaporite diapirs [27] on Axel Heiberg Island, including those in Expedition Fiord (Gypsum Hill Springs, GHS; 79°24′16″N; 90°43′52″W; 98 m.a.s.l.) and Colour Peak Diapir (CPS; 79°22′51″N; 91°16′09″W; 3 m.a.s.l.) (Figures 2 and 3(a)) and nearby Strand Fiord Wolf Diapir (WS; 79°4′36″N; 90°12′39″W; 132 m.a.sl.), not shown in Figure 2. Waters discharge either through numerous outlets or a single point source at constant rates and temperatures [3, 51], despite a mean annual air temperature of -15°C [1] and a lowest measured temperature of –54.6°C at a nearby weather station (Eureka, Nunavut, 1979) and measured permafrost thickness of 400–600 m [54].

Discharging spring waters are hypersaline, ranging from ~1 to 4 molal NaCl (4.7-18.9 wt% NaCl) [55, 56] (Table 2). Minerals including sulfates, carbonates, and halides have been documented in association with spring discharge, which form by a variety of disequilibrium processes including evapoconcentration and CO_2 degassing [55–58]. Icings (sheet-like masses of layered ice) form in distal areas during winter months when air and water temperatures are lowest, as well as carbonate and sulfate minerals thought to precipitate by freezing fractionation [51, 59]. At several sites, waters and sediments near spring outlets host microbial communities that are supported by carbon- and energy-rich reduced substrates including sulfur and methane [60–65]. The source and activity of spring discharge at Expedition Fiord (CPS, GHS) has been generally interpreted to represent recent phenomena related to periglacial processes [7], but this model cannot account for activity at Wolf Spring, which is located south of Strand Fiord south of the area shown in Figure 2 [57].

Andersen et al. [7, 50, 66] proposed a qualitative and quantitative model for the PSS that envisioned a relatively surficial circulation of fluids, with recharge from Astro and Phantom Lakes, which are located on the eastern flank of Thompson Glacier, ~397 m above the outlet of the springs (upper right corner, Figure 2; Phantom Lake is located east of Astro Lake, just outside the map in Figure 2). The above authors assumed that the deep subsurface salt layer acts as a reservoir and conduit of water. Seasonally, the lakes drain partially (1-2%) and the water would circulate to the PSS through faults, such as the ones mapped in the area (Figures 2 and 3). Water would flow below the surface at a depth of 600-700 m via an evaporite layer, returning to the surface through the piercement structures associated with the springs. Below the surface, the water would attain the geothermal temperature (they assumed a geothermal gradient of 37.3°C/km after [54]). As it flows upward, the brines would lose heat to the surrounding permafrost.

This study brings a new perspective to the interpretation and significance of the PSS.

5. Results

5.1. Perennial Springs at Colour Peak Diapir (CPS). Confirmed perennial spring activity is observed at three locations on western Axel Heiberg Island, two of which (Colour Peak and Gypsum Hill) are shown in Figure 2. They are among the most poleward perennial springs on Earth and are the only known example of cold, nonvolcanic springs in a region dominated by continuous permafrost. The two spring sites proximal to the hydrothermal development in Expedition Fiord are located adjacent to Colour Peak Diapir (CPS) and Expedition Diapir (GHS), with the springs at Wolf Diapir (WS) occurring ~60 km to the south.

Table 2 summarizes and compares the main geochemical and hydrological characteristics of these perennial springs. Groundwater emerges from either a single outlet or numerous seeps and springs (~40 at GHS, ~30 at CPS; [57]) resulting in total site discharge flow rates of 4–25 L/s. Discharge temperatures range from~ -6°C to ~ +6°C, but a review of past work suggests that outlet temperatures have remained constant (±2°C). The outlet waters have varying pH (5.8–7.4) but with high reducing potential (-171 to -312 mV) and low dissolved oxygen (0.2–0.5%). While concentrations of ionic constituents vary between sites, the waters are all Na-Cl-type brines (8-24% NaCl) with minor concentrations of Ca^{2+}, Mg^{2+}, K^+, SO_4^{2-}, NO_3^-, and HCO_3^-. Low concentrations of Fe^{2+}, NH_4^+, and HS^- have been measured in the discharging waters.

A notable aspect that differentiates the CPS from GHS is elevated P_{CO2} in waters at CPS, which results in the oversaturation and subsequent precipitation of calcite (travertine) by CO_2 degassing [55]. Travertine precipitation (Figure 5(a)) in narrow valleys form channels, which were initially described as being composed of alternating light (calcite spar) and dark (anhedral microcrystalline calcite combined with organic matter and noncarbonate minerals) laminae enriched in Fe, S, Na, and Si (Figure 5(b), [55]). Synchrotron radiation-based μ-XFM mapping across several of these micritic laminae (Figure 6) confirm the presence of Fe but also detect smaller concentrations of Mn, Zn, Cu, and Ni. A closer inspection of laminae within the calcite fabric by SEM shows two kinds of micritic fabrics: microcrystalline FeS grains and abrupt boundary layers (Figures 5(c)–5(f)). FIB-SEM imaging of a region encompassing both micritic fabrics reveal trapped gas bubbles associated with cavitating brines, FeS grains embedded within the calcite matrix, and the boundary layer (Figures 5(g)–5(j)). These microcrystalline FeS grains are similar in morphology to fine-grained sediment collected at spring outlets that are composed of small (0.1 μM) aggregates of FeS microcrystals (Figures 5(k) and 5(l)).

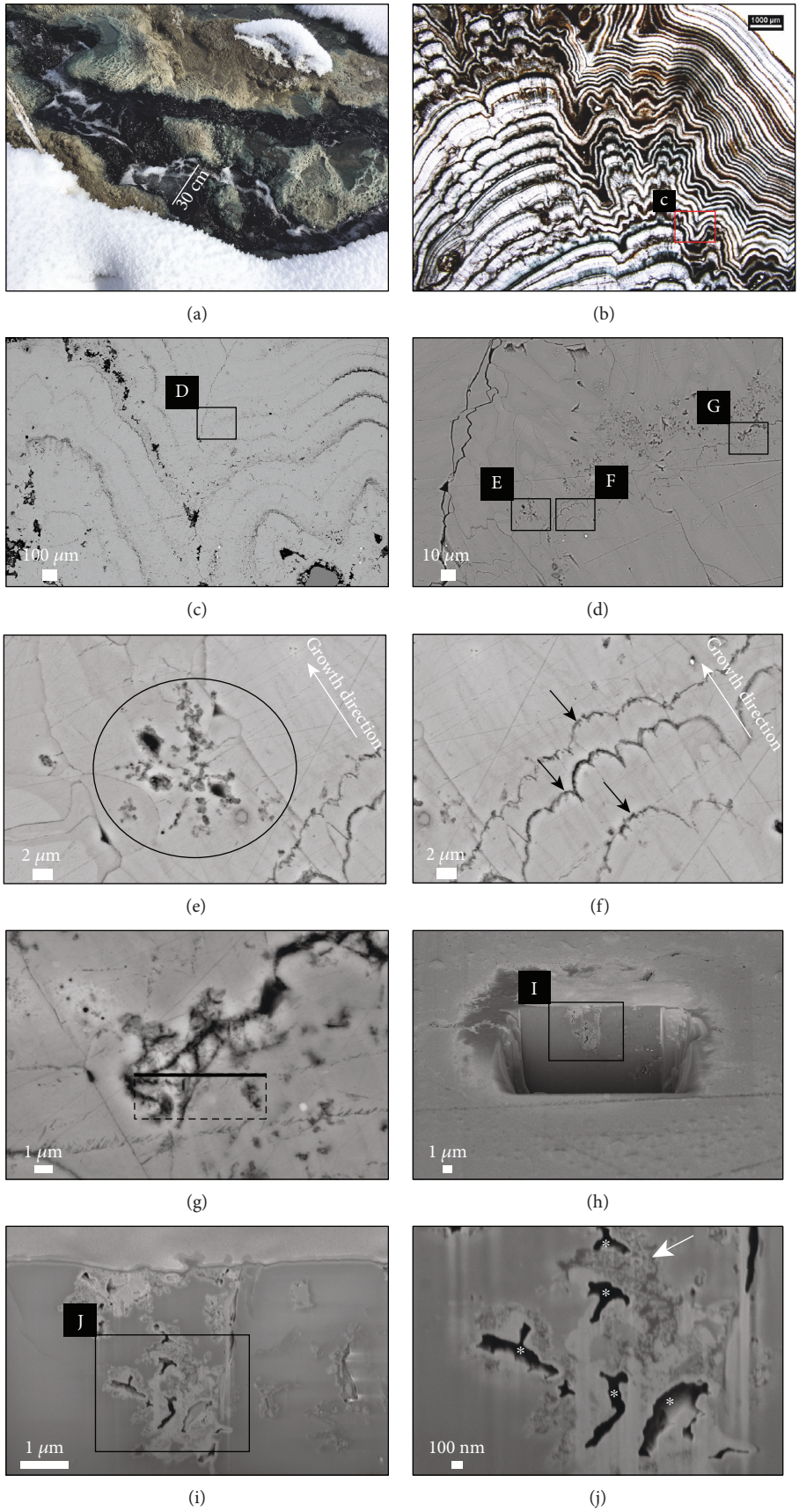

Figure 5: Continued.

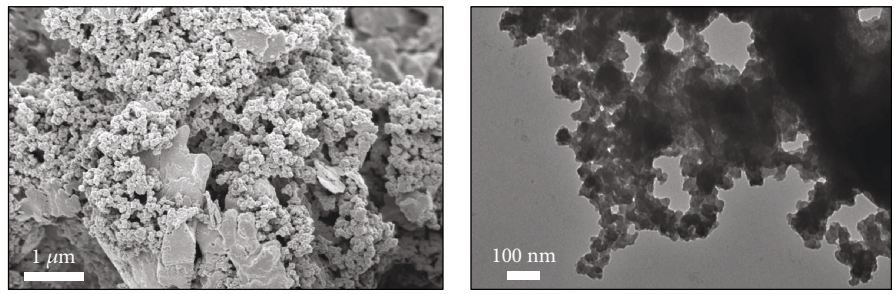

(k) (l)

Figure 5: (a) Example of channel-forming travertine at CPS. Photo taken May 2018; channel bounded by snow. (b) Double-polished thin section of channel travertine overhang showing laminated fabric. (c) SEM-BSD micrograph of area shown in (b). (d) SEM-BSD micrograph of area shown in (c). (e, f) SEM-BSD micrographs of areas shown in (d) showing two types of micritic fabrics: (e) microcrystalline grains embedded within calcite (circle) and (f) abrupt boundary layers (arrows). (g) SEM-BSD micrograph of area shown in (d). Dashed square shows area milled in (h) with thick bar showing milled face. (h) SEM in-lens micrograph of FIB-milled face shown in (g). (i) SEM in-lens micrograph of area shown in (h). (j) SEM-SE micrograph of area shown in (i). Note trapped gas inclusions (asterisks) and microcrystalline grains (arrow) within the calcite matrix. (k) SEM in-lens micrograph of aggregates of microcrystalline FeS grains intermixed with surficial sediments from a CPS outflow. (l) TEM micrograph of microcrystalline FeS aggregates from a CPS outflow. Note morphological similarities to microcrystalline grains in (j).

While it was previously suggested that Fe-rich laminations result from precipitation of iron oxyhydroxides [e.g., Fe $(OH)_3{\cdot}nH_2O$; [55]], the combination of (1) accumulation of metals including Zn, Cu, and Ni; (2) morphological similarities between sediments observed in micritic laminate and spring outlets; and (3) the apparent absence of bacteria and/or biofilms in association with these sediments suggests that they are allochthonous. It is hypothesized that these sediments form as a by-product of subsurface sulfate-reducing bacteria that are subsequently entrained by groundwater and carried to the surface, where they accumulate in shallow outlet pools and are washed downstream and incorporated into the calcite fabric as micritic laminae during pulses of higher groundwater discharge.

5.2. Geological and Mineralogical Characteristics of the White Glacier vein array (WGVA). The WGVA forms a conspicuous brown gossan exposed on a steep western flank confining White Glacier (79°26.66′N; 90°42.20′W; 350 m.a.s.l.), covering an area of more than 350 × 50 m and a range of elevation of ca. 50 m (Figures 3(b) and 7(a)). The veins are likely to be present as well under the glacier. The WGVA includes veins, mineralized breccias, and carbonate masses with a variety of structures (Figure 7). The host rocks are a dark grey chaotic mass of tight, matrix-supported angular breccia with angular fragments of sandstone, siltstone, shale, argillaceous limestone, dolomitic limestone, anhydrite, and gypsum of sizes predominantly <10 cm; the rock is reminiscent of fault breccia. According to the geological map, these beds belong to the Lower Jurassic "Savik beds" and the Upper Jurassic Awingak Formation [27], but the rocks are a jumbled mass, like clastic deposits near advancing salt allochthons described as off-diapir debris flows [6, 67]. These breccias match the description of anomalous, commonly overpressured rubble (termed "gumbo" in the Gulf of Mexico), found beneath allochthonous salt sheets and canopies in petroleum basins (e.g., [68, 69]).

Across from the mineralized zone, there is a wide band of highly sheared and broken-up rusty diabase (a conspicuous gossan), along an extensive Cretaceous diabase sill that can be followed for ca. 4 km along a steep ridge as far as Colour Lake, which lies adjacent to the MARS camp, near Gypsum Hill (Figure 2).

Mineralization consists predominantly of calcite, but textural and crystal habit evidence indicates that the earliest generation of Ca carbonate (cal1) originally crystallized as the polymorph aragonite (*c.f.* [70]). However, the aragonite composition is not preserved and has reverted to calcite on the basis of Raman spectroscopic measurements that show none of the characteristic vibrations for aragonite ($142\,cm^{-1}$, $162\,cm^{-1}$, $190\,cm^{-1}$, $211\,cm^{-1}$, and $701\,cm^{-1}$) and, despite crystal habit, the three dominant vibration lines for calcite are present ($156\,cm^{-1}$, $281\,cm^{-1}$, and $712\,cm^{-1}$) in cal1. Minor quartz, locally barite and abundant iron sulfides pyrite and marcasite (orthorhombic dimorph *of* pyrite), with minor pyrrhotite, chalcopyrite, sphalerite, and galena are present. All the structures suggest "open-space filling" with minimal replacement, reminiscent of epithermal and epigenetic deposits formed at shallow depths. Epidote and chlorite are common where the veins intersect diabase from the mafic dike (Figure 7(c)), and clay minerals are visible in thin sections. The early generation of brown calcite (cal1; after aragonite) occurs in crustified veins, generally as acicular crystals lining fractures, or in radial crystal aggregates filling cavities or around rock fragments (Figure 7(d)). A second generation of calcite (white-orange, sparry; cal2) forms massive infillings with minor quartz, in the central parts of some veins (Figures 7(b) and 7(d)). Locally, there are clear crystals of Iceland spar of up to 10 cm in size. A common structure of calcite is banded "zebra rock" consisting of acicular calcite layers alternating with darker, cm-thick black, carbon-rich sedimentary laminae (Figures 7(e)–7(g)). The laminae are generally subhorizontal but locally contorted, showing variable inclined or vertical orientations in single exposures

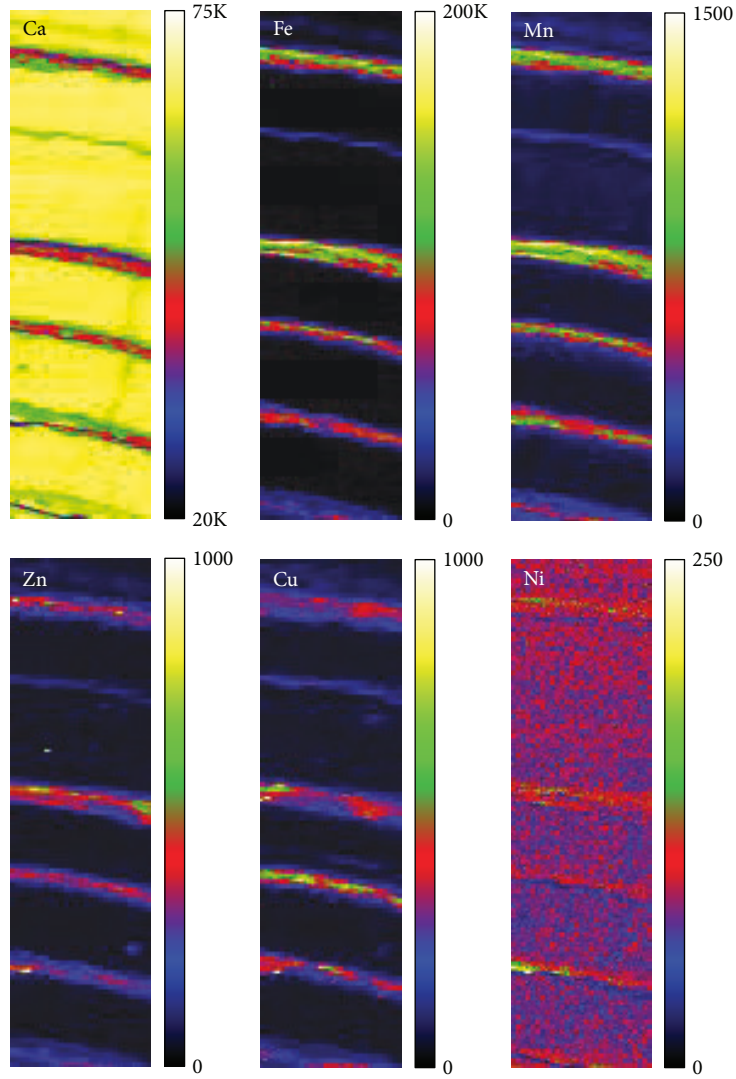

Figure 6: μ-XFM of laminated calcite forming in CPS discharge at Colour Peak Diapir. Qualitative concentrations shown as intensities in counts per second from low (black) to high (white). Intensity ranges denoted by scale bars for each element. The vertical scale of each map is 500 μm.

(Figure 7(f)), probably tectonically disrupted. Sulfides occur in darker laminae within the aggregates, in veins and as botryoidal aggregates filling large open cavities (Figures 7(g) and 7(h)). Sulfides visible in hand sample are pyrite and marcasite.

Under the reflected light microscope, pyrite occurs as subhedral to euhedral crystals of highly variable grain size (<1 mm to >1 cm), locally with cataclastic structure (Figures 8(a) and 8(b)). Marcasite was distinguished from pyrite by its conspicuous anisotropy and its commonly rosette or tabular habit, but in many samples both minerals occur together in rosettes, or plumose structures (Figures 8(c) and 8(d)) with alternating marcasite- and pyrite-rich bands. Some marcasite shows only faint anisotropy. Anhedral pyrite shows considerable porosity and minor remnant anisotropy, which may be the result of conversion from marcasite [71]; it probably crystallized as marcasite and was converted to pyrite in response to hydrothermal heating. Rare grains of galena, sphalerite (Figure 8(e)) and chalcopyrite, pyrrhotite, and arsenopyrite are observed as minute crystals hosted in early brown carbonate (cal1), locally close to the margins of the veins, within them or in the adjacent host. Pyrite framboids (5-8 μm in diameter and made of cubic or octahedral pyrite microlites of 1-2 μm) occur within black (organic-carbon rich) bands within laminated carbonate (Figure 8(f)). Some framboid aggregates appear to have partially recrystallized into euhedral pyrite (Figure 8(g)) but retain internal porosity filled with impurities.

Under the electron microprobe, pyrite (30 spot analyses) and marcasite (11 spot analyses) are compositionally indistinguishable and show a range of impurities, from below detection to maximum (in wt %) as follows: Mn (avg. 0.11%; max. 1.22%), Ni (avg. 0.03%; max. 0.23%), Co

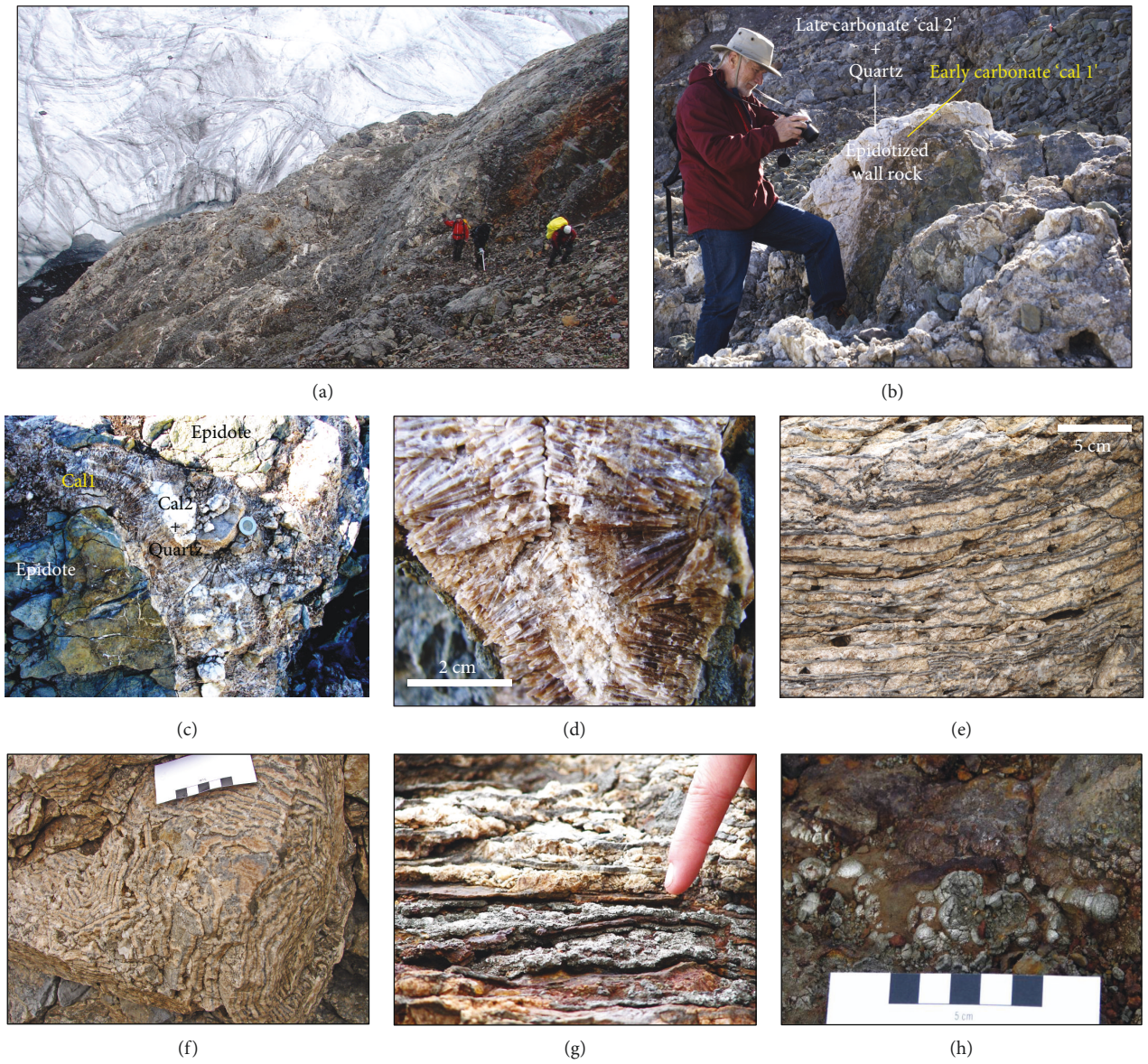

Figure 7: Outcrop-scale features of the WGVA site. (a) Partial overview of the site showing metal gossan (upper left) and hydrothermal veining in wallrock. (b) Outcrop within the exposure in (a) containing zoned calcite-quartz vein hosted in partial epidotized wallrock showing the relative size of vein structures (M. Zentilli for scale). (c) Individual vein showing early brown carbonate ("cal1") crystals symmetrically lining wallrock contacts, with a vuggy infilling white (sparry) calcite ("cal2") and quartz. Epidotized wallrock containing minor secondary vein splays occurs in the vein selvage. (d) Enlarged view of vein showing early brown carbonate crystals radiating from vein margins symmetrically towards the vein centre containing euhedral terminations and open space in this example. (e) "Zebra" texture showing alternating layers of carbonate- and sulfide-rich hydrothermal mineralization (white-tan) with wall-rock septae (grey). (f) Contorted "zebra" texture indicating post-crystallization deformation. (g) Enlarged view of sulfide-rich host rock layers separated by hydrothermal carbonate. (h) Botryoidal masses of pyrite-marcasite.

(<0.04%), Pb (avg. 0.06%; max. 0.26%), Cd (avg. 0.04%; max. 0.29%), Zn (avg. 0.01%; max. 0.08%), Cu (avg. 0.01%; max. 0.08%), Ag (avg. 0.002%; max. 0.02%), and As (avg. 0.003%; max 0.053%). Traces of Au were detected in some sulfide analyses but remain unconfirmed. Visibly zoned crystals ($n = 7$) were analyzed at their centres and margins; while no consistent compositional patterns were detected, on average the centres have one order of magnitude more As, Mn, and Ni and are depleted in Cd. Apart from carbonates, qualitative evidence for the presence of titanite, barite, and other sulphates was found, as well as Fe and Ti oxides with varying amounts of Mn.

Pyrite framboids are difficult to analyze because the microprobe beam is larger than the microlites, and low-density interstitial material (possibly organic matter or volatile minerals) contaminates the analyses, and totals are low; thus, the results are only qualitative. Prominent impurities in framboid analyses ($n = 7$) are Mn (avg. 0.15%; max. 0.60%), Pb (avg. 0.123%; max. 0.158%), Ni (avg. 0.09%; max. 0.19%), Cd (avg. 0.014%; max. 0.044%), Zn (avg.

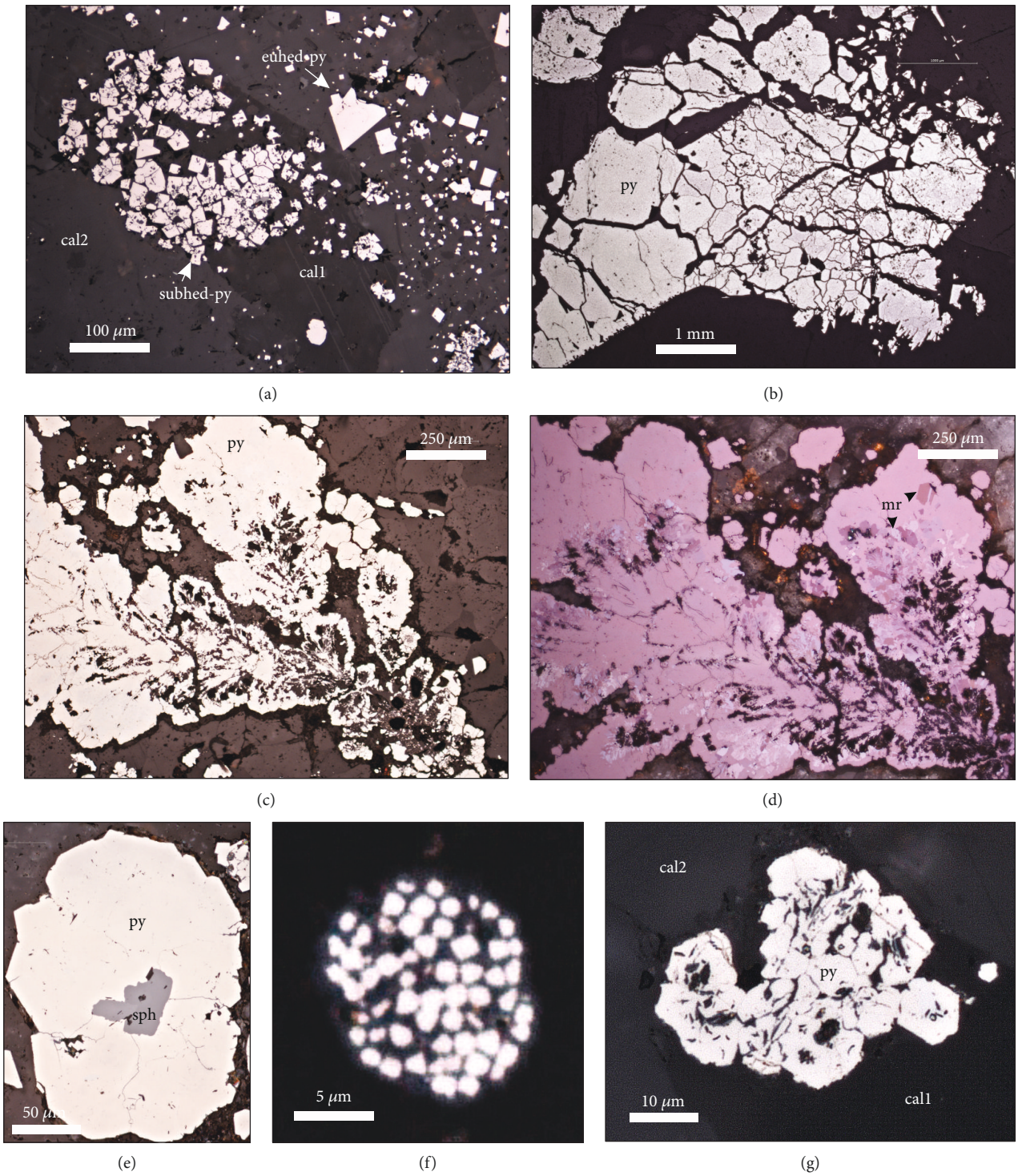

Figure 8: Reflected light photomicrographs summarizing textural and compositional characteristics of sulfides in vein margins associated with vein carbonates and laminated sedimentary wall rocks. (a) Recrystallized (former framboids) subhedral pyrite (subhed-py) in early brown carbonate ("cal 1") surrounded in later carbonate ("cal 2") containing euhedral pyrite (euhed-py). (b) Cataclastic pyrite in wall rock. (c-d) Plumose, porous, pyrite-marcasite intergrowths showing massive domains of pyrite alternating with polycrystalline domains of marcasite. (d) Same area as (c) but in crossed nicols to emphasize anisotropy of marcasite; enclosed dark material is calcite. Dark areas within pyrite-marcasite intergrowths are porosity. (e) Subhedral pyrite polycrystalline aggregate with sphalerite core. (f) Pyrite framboid in black layer of "zebra" rock (Figure 7(g)). (g) Recrystallised pyrite (former framboid) along vein-wallrock margin enclosed within early brown carbonate domain ("cal 1").

Table 3: Selected trace element concentrations from paleospring carbonates.

Ablation #	[1]Phase	Fe_2O_3 *wt.%*	MnO *wt.%*	MgO *wt.%*	Sr *μg/g*	Ba *μg/g*	La *μg/g*	Ce *μg/g*	Yb *μg/g*	Lu *μg/g*	Pb *μg/g*	Zn *μg/g*	Cu *μg/g*	Sr/Ca	[2]La_N/Yb_N
10au20e03.xl	cal2	0.034	0.361	0.023	341	0.50	0.71	1.30	0.04	b.d.l.	0.35	b.d.l.	0.10	0.0262	1.48
10au20e04.xl	cal2	0.025	0.493	0.014	125	0.53	b.d.l.	b.d.l.	b.d.l.	b.d.l.	0.15	0.21	b.d.l.	0.0096	-
10au20e05.xl	cal2	0.025	0.517	0.014	116	b.d.l.	b.d.l.	b.d.l.	b.d.l.	b.d.l.	0.33	0.16	0.06	0.0089	-
10au20e07.xl	cal2	0.011	0.287	0.011	29	0.96	2.08	2.20	0.08	0.01	0.17	b.d.l.	b.d.l.	0.0023	2.02
10au20e08.xl	cal2	0.032	0.347	0.023	252	0.41	0.66	0.86	b.d.l.	b.d.l.	1.14	b.d.l.	b.d.l.	0.0193	-
10au20e09.xl	cal2	0.034	0.377	0.021	483	2.54	0.72	1.22	0.04	0.01	0.41	0.13	b.d.l.	0.0370	1.33
10au20e10.xl	cal2	0.029	0.314	0.016	406	1.54	0.61	1.04	b.d.l.	b.d.l.	0.19	b.d.l.	0.12	0.0311	-
10au20f03.xl	cal2	0.010	0.321	0.031	349	9.31	0.62	0.98	b.d.l.	b.d.l.	0.71	0.64	0.13	0.0268	-
10au20f04.xl	cal2	0.011	0.424	0.042	175	12.00	0.27	0.41	b.d.l.	b.d.l.	1.22	0.75	0.15	0.0134	-
10au20f06.xl	cal2	0.008	0.340	0.038	214	6.96	0.49	0.69	b.d.l.	b.d.l.	6.74	2.66	0.56	0.0164	-
10au20f07.xl	cal2	0.011	0.368	0.033	224	8.21	0.54	0.74	b.d.l.	b.d.l.	0.56	0.43	b.d.l.	0.0172	-
10au20f08.xl	cal2	0.009	0.409	0.036	122	2.24	0.27	0.27	b.d.l.	b.d.l.	0.12	b.d.l.	b.d.l.	0.0093	-
10au20f09.xl	cal2	0.011	0.418	0.048	264	1.50	0.48	0.52	b.d.l.	b.d.l.	0.49	b.d.l.	0.62	0.0202	-
10au20f10.xl	cal2	0.006	0.419	0.038	265	19.82	0.59	0.67	b.d.l.	b.d.l.	3.43	b.d.l.	b.d.l.	0.0203	-
10au20f11.xl	cal2	0.014	0.413	0.044	265	17.53	0.23	0.52	b.d.l.	b.d.l.	3.51	2.04	b.d.l.	0.0203	-
10au20f12.xl	cal2	0.012	0.421	0.056	323	45.67	0.88	1.10	0.12	b.d.l.	0.38	0.36	0.21	0.0248	0.53
10au20f13.xl	cal2	0.010	0.446	0.036	56	b.d.l.	0.08	0.06	b.d.l.	b.d.l.	0.37	0.49	b.d.l.	0.0043	-
10au20f14.xl	cal2	0.011	0.462	0.038	50	b.d.l.	0.01	0.04	b.d.l.	b.d.l.	0.08	b.d.l.	b.d.l.	0.0038	-
10au20d03.xl	cal2	0.009	0.410	0.169	203	2.80	0.04	0.07	b.d.l.	0.02	0.44	b.d.l.	b.d.l.	0.0156	-
10au20d04.xl	cal2	0.012	0.450	0.164	222	15.34	0.08	b.d.l.	b.d.l.	b.d.l.	2.01	2.07	b.d.l.	0.0170	-
10au20d05.xl	cal2	0.012	0.417	0.140	214	19.37	b.d.l.	0.15	b.d.l.	b.d.l.	3.03	b.d.l.	b.d.l.	0.0164	-
10au20d06.xl	cal2	0.011	0.480	0.151	248	13.11	0.04	0.10	0.14	0.02	2.22	0.80	0.25	0.0190	0.02
10au20d07.xl	cal1	0.010	0.268	0.066	925	774.59	0.33	0.55	0.17	0.02	0.12	b.d.l.	0.46	0.0709	0.14
10au20d08.xl	cal1	0.010	0.313	0.076	940	606.54	0.34	0.68	0.16	b.d.l.	6.13	2.58	0.40	0.0721	0.16
10au20d09.xl	cal1	0.010	0.299	0.082	990	767.47	0.31	0.64	0.11	0.01	4.42	1.28	0.67	0.0759	0.20
10au20d10.xl	cal1	0.008	0.246	0.052	868	527.30	0.27	0.59	b.d.l.	b.d.l.	5.28	1.28	0.68	0.0666	-
10au20d11.xl	cal1	0.009	0.286	0.063	905	546.52	0.31	0.64	0.16	0.01	1.24	0.56	0.26	0.0694	0.14
10au20d12.xl	cal1	0.008	0.260	0.052	867	556.46	0.32	0.56	0.16	0.02	0.43	0.69	0.42	0.0665	0.15
10au20d13.xl	cal1	0.009	0.287	0.059	937	556.73	0.27	0.66	0.08	0.01	0.68	0.98	0.26	0.0719	0.25
10au20d14.xl	cal1	0.009	0.242	0.055	893	578.83	0.32	0.51	0.09	0.02	0.76	1.00	0.43	0.0685	0.25
10au20d15.xl	cal1	0.010	0.251	0.059	926	621.45	0.32	0.63	0.12	0.02	0.50	0.88	0.53	0.0710	0.20
10au20d16.xl	cal1	0.009	0.269	0.081	846	583.22	0.26	0.67	0.14	0.01	1.00	2.48	0.55	0.0649	0.13

Notes: [1]cal 2 = white/orange infilling sparry calcite; cal 1 = brown calcite lining vein wall; [2]REE normalized to PAAS.

0.006%; max. 0.021%), Cu (avg. 0.009%; max. 0.034%), and As (avg. 0.0175%; max. 0.053%).

One crystal of pyrrhotite was encountered with 0.06% Cu. One arsenopyrite grain was encountered that showed detectable Pb, Co, Ni, Zn, and Ag.

5.2.1. Trace Elements in Carbonate. Selected trace elements in cal1 and cal2 are listed in Table 3. Early brown acicular calcite has a hexagonal crystal form and elevated Sr, Ba, and Mg compared to sparry white-orange calcite. If abundant in the associated fluid, these ions are known to stabilize aragonite [72], which may have reverted to calcite as the hydrothermal fluid became diluted with time or warmer (*c.f.* [73]). Strontium and Ba are variable in concentration but reach concentrations as high as ~1000 ppm and ~770 ppm, respectively, with Sr and Ba showing a positive correlation, consistent with their precipitation from a fluid derived from dissolution of marine carbonates. In the absence of secondary dolomitization, lower Sr values emphasize meteoric water dilution. LREE/HREE ratios (e.g., PAAS normalized La/Yb) are $\ll 1$ for carbonate analyses with Sr > 800 ppm, also diagnostic of hydrothermal carbonate precipitated from seawater or a fluid that interacted with, or dissolved, marine carbonate (*c.f.*, [70]). Elevated concentrations of Ba likely indicate that small inclusions of the mineral witherite ($BaCO_3$) are present as such high concentrations would not be present as dissolved Ba in the Ca-carbonate structure. Elevated concentrations of Pb, Zn, and Cu are likely not dissolved concentrations but rather indicate the presence of very small particles of included, coprecipitated or secondary sulfide minerals (e.g., galena, sphalerite, and chalcopyrite). Petrographic observation of trace quantities of these sulfides within veins and host

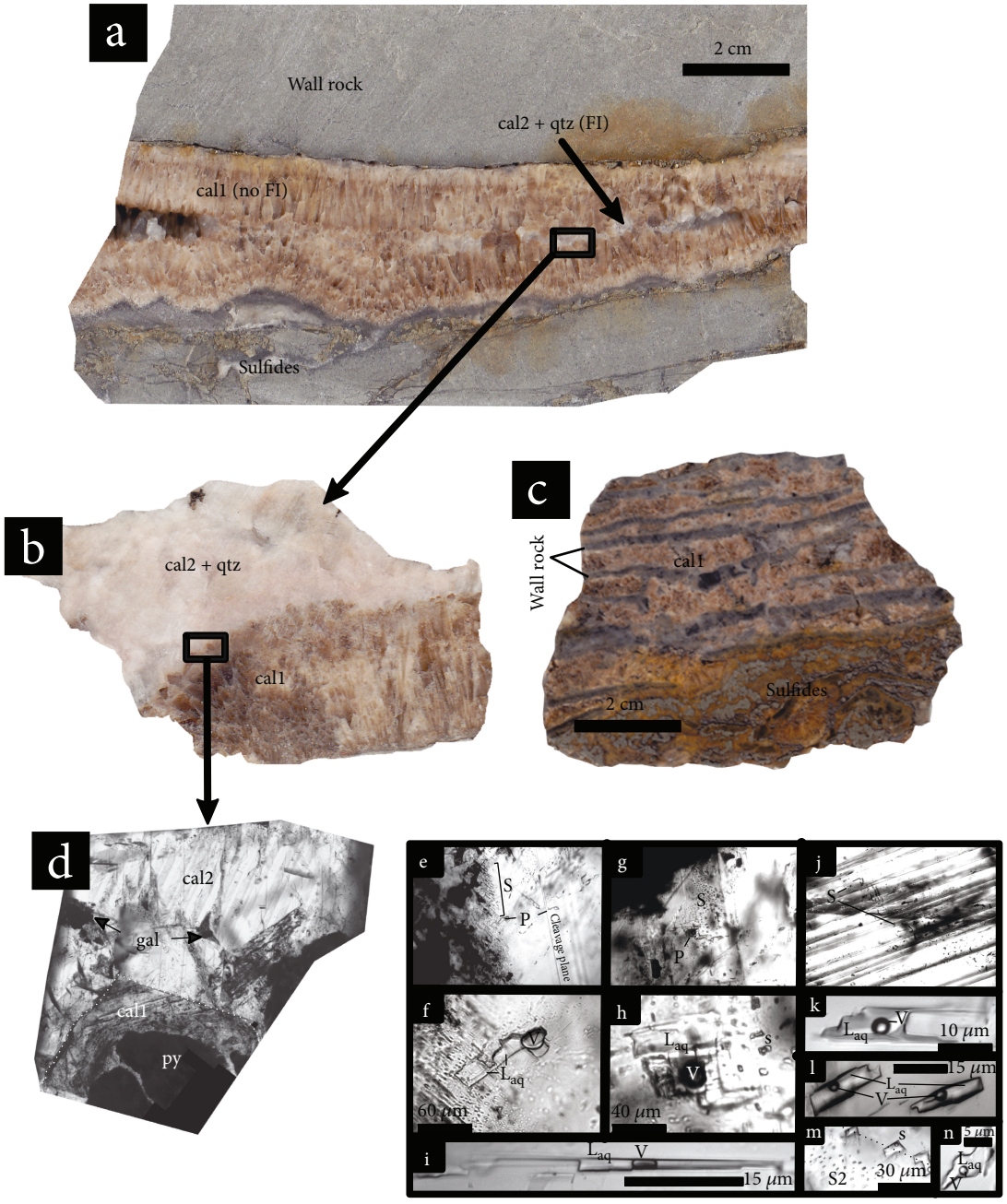

Figure 9: Petrographic characteristics of carbonate-quartz veins (WGVA). (a) Complete vein cross section (hand sample) showing early brown, comb-textured (acicular, hexagonal) carbonate lining vein wall (cal1), later white, massive, sparry carbonate and quartz (cal2 + qtz), and sulfide-mineralized wallrock. (b) Enlarged view of the contact between cal1 and cal2 generations where euhedral crystals of cal1 contact cal2. (c) Banded ("zebra") texture showing alternating layers consisting of sulfide-mineralized wall rock laminae and cal2. (d) Thin-section photomicrograph (transmitted light) showing the paragenetic sequence of early pyrite (py) surrounded in zoned, euhedral brown carbonate (cal1), followed by massive white-orange carbonate (cal2) infilling and late galena infilling fractures and pits in cal2. (e-h) Transmitted light (ppl) photomicrographs (at 20°C) showing large primary ("P") two-phase ($L_{aq} + V$) inclusions and planes of much smaller secondary ("S") two-phase ($L_{aq} + V$) inclusions in cal2. Images (f) and (h) show more highly magnified areas of the central parts of images (e) and (g), respectively. (i) Transmitted light (ppl) photomicrograph (at 20°C) of a long, rectangular primary two-phase ($L_{aq} + V$) inclusion in cal2. (j) Transmitted light (ppl) photomicrograph (at 20°C) of a planar trail of secondary inclusions cross-cutting cal2 cleavage planes. (k-l) Secondary fluid inclusions in cal2 containing two phases ($L_{aq} + V$) at 20°C. (m) Transmitted light (ppl) photomicrograph (at 20°C) of an irregularly shaped secondary two-phase inclusion ($L_{aq} + V$) in cal1. (n) Transmitted light (ppl) photomicrograph (at 20°C) shows two types of secondary inclusion morphologies in cal2: rectangular to irregular two-phase inclusions ("S") and later ("S2") rectangular two-phase inclusions with rounded edges. The latter inclusions tend to show lower T_h values (see text for description).

Table 4: Microthermometric data for paleocarbonate-hosted fluid inclusions from Striae Hill and White Glacier.

FIA	Stage	Location	Sample	Origin	T_m^{ice} (°C)	Salinity	T_h (°C)	FIA	Stage	Location	Sample	Origin	T_m^{ice} (°C)	Salinity	T_h (°C)
A	cal2	Striae Hill	SF05-3E	S	-0.7	1.2	n.m.	O	cal2	White Glacier	SF07-1	S	-9.8	13.8	146.9
A	cal2	Striae Hill	SF05-3E	S	-1.0	1.7	n.m.	O	cal2	White Glacier	SF07-1	S	-10.9	14.9	135.8
A	cal2	Striae Hill	SF05-3E	S	-0.6	1.1	n.m.	O	cal2	White Glacier	SF07-1	S	-9.4	13.3	178.6
A	cal2	Striae Hill	SF05-3E	S	-0.8	1.4	n.m.	P	cal2	White Glacier	SF07-1	S	-11.6	15.6	251.2
A	cal2	Striae Hill	SF05-3E	S	-0.7	1.2	n.m.	P	cal2	White Glacier	SF07-1	S	-9.1	13.0	192.5
A	cal2	Striae Hill	SF05-3E	S	-0.4	0.7	n.m.	Q	cal2	White Glacier	SF07-1	S	-7.8	11.5	192
A	cal2	Striae Hill	SF05-3E	S	-0.7	1.2	n.m.	Q	cal2	White Glacier	SF07-1	S	-5.2	8.1	228.1
A	cal2	Striae Hill	SF05-3E	S	-0.6	1.1	n.m.	Q	cal2	White Glacier	SF07-1	S	-5.2	8.1	167.8
A	cal2	Striae Hill	SF05-3E	S	-1.1	1.9	252.4	Q	cal2	White Glacier	SF07-1	S	-4.6	7.3	172.4
A	cal2	Striae Hill	SF05-3E	S	-0.9	1.6	155.6	Q	cal2	White Glacier	SF07-1	S	-1.8	3.0	192.7
A	cal2	Striae Hill	SF05-3E	S	-0.5	0.9	295.5	Q	cal2	White Glacier	SF07-1	S	-6.1	9.3	205.9
A	cal2	Striae Hill	SF05-3E	S	-0.5	0.9	270	R	cal2	White Glacier	SF07-1	S	-3	4.9	194.1
A	cal2	Striae Hill	SF05-3E	S	-1.0	1.7	n.m.	R	cal2	White Glacier	SF07-1	S	-1.9	3.2	220.6
A	cal2	Striae Hill	SF05-3E	S	-1.0	1.7	238.8	R	cal2	White Glacier	SF07-1	S	-5.2	8.1	232.9
A	cal2	Striae Hill	SF05-3E	S	-1.1	1.9	238.3	S	cal2	White Glacier	SF07-1	S	-1.3	2.2	202.2
B	cal2	Striae Hill	SF05-3E	P	-7.3	10.8	152.5	T	cal2	White Glacier	SF07-1	S	-0.2	0.2	232.8
C	cal2	Striae Hill	SF05-3E	S	-0.8	1.4	n.m.	T	cal2	White Glacier	SF07-1	S	-0.3	0.4	249.4
C	cal2	Striae Hill	SF05-3E	S	-0.6	1.1	n.m.	T	cal2	White Glacier	SF07-1	S	-0.3	0.5	250.2
D	cal2	Striae Hill	SF05-3E	S	-1.1	1.9	253.1	T	cal2	White Glacier	SF07-1	S	-0.3	0.4	224.6
D	cal2	Striae Hill	SF05-3E	S	-1.0	1.7	238.9	U	cal2	White Glacier	SF07-1	S	-0.2	0.2	199.7
D	cal2	Striae Hill	SF05-3E	S	-0.9	1.6	155.4	U	cal2	White Glacier	SF07-1	S	-0.2	0.2	174.6
E	cal2	Striae Hill	SF05-3E	S	-0.5	0.9	270.2	U	cal2	White Glacier	SF07-1	S	-0.3	0.4	163.2
E	cal2	Striae Hill	SF05-3E	S	-0.5	0.9	296.1	U	cal2	White Glacier	SF07-1	S	-0.3	0.4	155.3
F	cal2	Striae Hill	SF05-3E	P	-7.3	10.8	152.9	U	cal2	White Glacier	SF07-1	S	-0.3	0.5	111.5
G	cal2	White Glacier	SF07-1	P	-10.7	14.7	n.m.	V	cal2	White Glacier	SF07-1	S	-1.2	2.1	247.2
G	cal2	White Glacier	SF07-1	P	-7.2	10.7	n.m.	W	cal2	White Glacier	SF07-1	P	-11.5	15.4	155.7
G	cal2	White Glacier	SF07-1	P	-13.8	17.6	n.m.	W	cal2	White Glacier	SF07-1	P	-11.5	15.4	159.5
G	cal2	White Glacier	SF07-1	P	-11.5	15.5	231.5	X	cal2	White Glacier	SF07-1	P	-11.7	15.6	217.1
G	cal2	White Glacier	SF07-1	P	-11.5	15.5	156.1	X	cal2	White Glacier	SF07-1	P	-11.5	15.5	230.8
G	cal2	White Glacier	SF07-1	P	-11.4	15.4	159.7	X	cal2	White Glacier	SF07-1	P	-11.5	15.4	262.2
H	cal2	White Glacier	SF07-1	S	-1.1	1.9	n.m.	Y	cal2	White Glacier	SF07-1	P	-11.5	15.5	216.3
I	cal2	White Glacier	SF07-1	P	-10.1	14.0	n.m.	Y	cal2	White Glacier	SF07-1	P	-11.5	15.5	n.m.
I	cal2	White Glacier	SF07-1	P	-11.4	15.4	n.m.	Y	cal2	White Glacier	SF07-1	P	-11.5	15.5	n.m.
I	cal2	White Glacier	SF07-1	P	-11.5	15.5	262.8	Y	cal2	White Glacier	SF07-1	P	-11.5	15.5	n.m.
J	cal2	White Glacier	SF07-1	S	0.0	0.0	n.m.	Y	cal2	White Glacier	SF07-1	P	-11.5	15.5	n.m.

Table 4: Continued.

FIA	Stage	Location	Sample	Origin	T_m^{ice} (°C)	Salinity	T_h (°C)	FIA	Stage	Location	Sample	Origin	T_m^{ice} (°C)	Salinity	T_h (°C)
J	cal2	White Glacier	SF07-1	S	-0.2	0.4	n.m.	Y	cal2	White Glacier	SF07-1	P	-16.8	20.1	n.m.
J	cal2	White Glacier	SF07-1	S	0.0	0.0	177.2	Z	cal2	White Glacier	SF07-4	S	0.0	0.0	182.4
J	cal2	White Glacier	SF07-1	S	-0.1	0.2	233	Z	cal2	White Glacier	SF07-4	S	-0.3	0.5	112.1
J	cal2	White Glacier	SF07-1	S	-0.2	0.4	225.3	Z	cal2	White Glacier	SF07-4	S	-0.1	0.2	200.9
J	cal2	White Glacier	SF07-1	S	-0.1	0.2	174.9	Z	cal2	White Glacier	SF07-4	S	-1.3	2.2	n.m.
J	cal2	White Glacier	SF07-1	S	-1.2	2.1	246.9	Z	cal2	White Glacier	SF07-4	S	-0.1	0.2	n.m.
J	cal2	White Glacier	SF07-1	S	-0.3	0.5	250	Z	cal2	White Glacier	SF07-4	S	-1.0	1.7	n.m.
J	cal2	White Glacier	SF07-1	S	0.0	0.0	176.4	Z	cal2	White Glacier	SF07-4	S	-0.5	0.9	n.m.
K	cal2	White Glacier	SF07-1	S	-0.7	1.2	n.m.	Z	cal2	White Glacier	SF07-4	S	-1.3	2.2	n.m.
K	cal2	White Glacier	SF07-1	S	-1.4	2.4	n.m.	Z	cal2	White Glacier	SF07-4	S	-2.3	3.9	n.m.
K	cal2	White Glacier	SF07-1	S	-0.2	0.4	249.8	Z	cal2	White Glacier	SF07-4	S	-0.1	0.2	n.m.
K	cal2	White Glacier	SF07-1	S	-0.2	0.4	155.3	AA	cal2	White Glacier	SF07-4	P	-11.5	15.5	n.m.
K	cal2	White Glacier	SF07-1	S	-0.2	0.4	163.7	AA	cal2	White Glacier	SF07-4	P	-11.5	15.5	n.m.
L	cal2	White Glacier	SF07-1	S	-5.8	8.9	192.1	AA	cal2	White Glacier	SF07-4	P	-9.9	13.7	n.m.
L	cal2	White Glacier	SF07-1	S	-5.7	8.8	189.4	BB	cal1	White Glacier	SF07-1	S	n.m.	n.m.	308.2
L	cal2	White Glacier	SF07-1	S	-5.8	8.9	158.5	BB	cal1	White Glacier	SF07-1	S	n.m.	n.m.	297.9
M	cal2	White Glacier	SF07-1	S2	-3.3	5.4	125.3	BB	cal1	White Glacier	SF07-1	S	n.m.	n.m.	290.8
N	cal2	White Glacier	SF07-1	S	-3.3	5.4	144.5	CC	cal1	White Glacier	SF07-1	S	-8.3	12.1	264.8
N	cal2	White Glacier	SF07-1	S	-1.2	2.1	144	CC	cal1	White Glacier	SF07-1	S	-8.3	12.1	270.6
N	cal2	White Glacier	SF07-1	S	-2.2	3.7	137.6	DD	cal1	White Glacier	SF07-1	S	-16.9	19.8	215
N	cal2	White Glacier	SF07-1	S	-0.4	0.7	166.2	EE	cal1	White Glacier	SF07-1	S	-1.4	2.4	137.4
O	cal2	White Glacier	SF07-1	S	-9.5	13.4	193.3	EE	cal1	White Glacier	SF07-1	S	-1.2	2.1	208.4
O	cal2	White Glacier	SF07-1	S	-9.3	13.2	149.1	EE	cal1	White Glacier	SF07-1	S	-0.9	1.6	158.8
O	cal2	White Glacier	SF07-1	S	-9.5	13.4	164.3	EE	cal1	White Glacier	SF07-1	S	-1.1	1.9	175.6
O	cal2	White Glacier	SF07-1	S	-10.4	14.4	126.5	EE	cal1	White Glacier	SF07-1	S	-0.6	1.1	162.1

Notes: Salinity reported in wt% NaCl equivalent. FIA = fluid inclusion assemblage; S/S2 = secondary origin; P = primary; T_m^{ice} = final ice melting T; Th = homogenization T (L + V to L); n.m. = not measured.

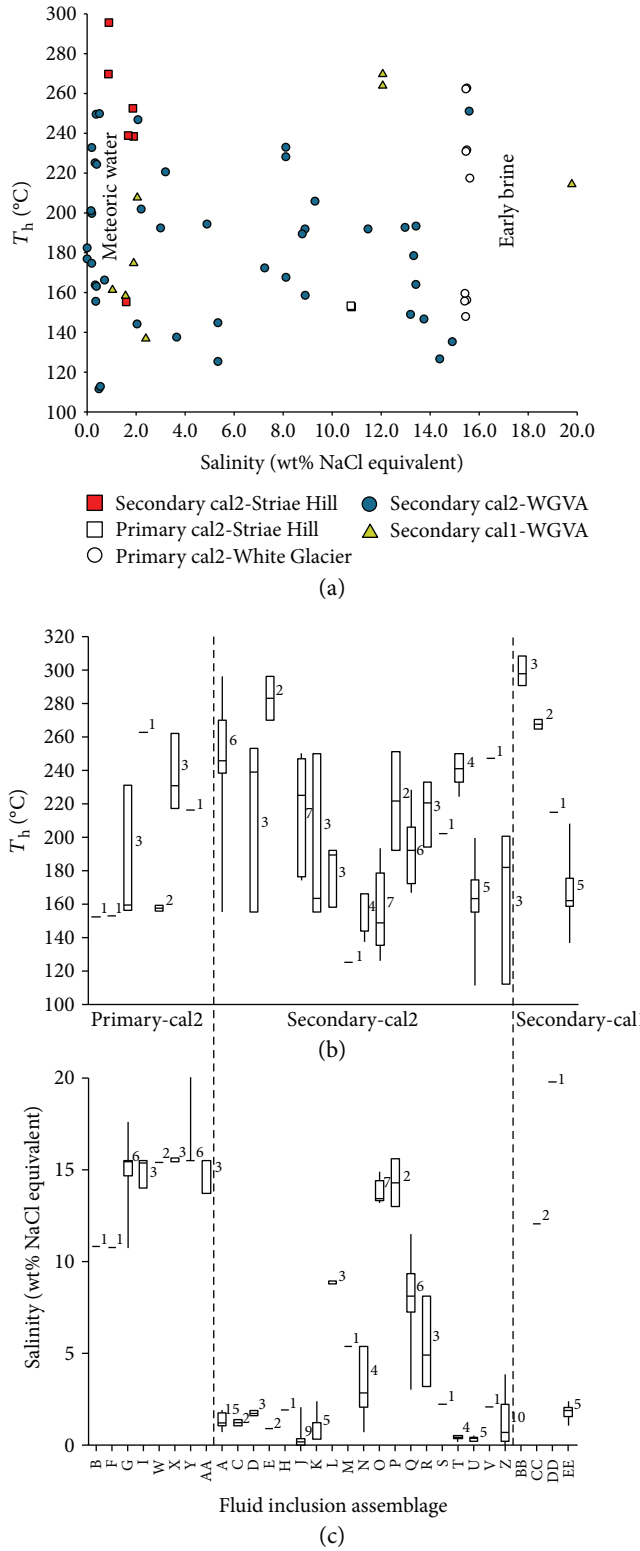

Figure 10: Microthermometric data for primary and secondary fluid inclusions in carbonates from the paleosprings (WGVA and Striae Hill sites). (a) Summary of all data (T_h vs. bulk salinity) for primary and secondary inclusions in carbonates from WGVA and Striae Hill sites. Note the lack of correlation between T and salinity, and the continuum in bulk salinity from a high-salinity brine in the earliest inclusions to variable salinity fluid (brine to meteoric range) in secondary inclusions. (b-c) Box-whisker plots summarizing microthermometry data for primary and secondary inclusions organized by fluid inclusion assemblage. Numbers next to box-whisker markers indicate the number of inclusions in each measured assemblage. Single assemblages can show up to a ~150°C intra-assemblage range in homogenization by vapour bubble disappearance, attributed to post-entrapment modification (leakage, necking down).

Table 5: Stable S-O-C analyses of mineral separates from modern spring/paleospring, and [1]calculated water $\delta^{18}O$.

Sample	Setting	Mineral phase	Measured (mineral ‰)			Calculated (fluid ‰)		
			$\delta^{34}S_{VCDT}$	$\delta^{18}O_{VSMOW}$	$\delta^{13}C_{VPDB}$	$\delta^{18}O_{H2O}$	$\delta^{18}O_{H2O}$	$\delta^{18}O_{H2O}$
						6°C	150°C	300°C
SF-10	Paleospring	Pyrite	-2.7	-	-	-	-	-
SF-14	Paleospring	Pyrite	1.7	-	-	-	-	-
SF-14	Paleospring	Pyrite	16.4	-	-	-	-	-
SF-15	Paleospring	Pyrite	11.4	-	-	-	-	-
COS1	Modern spring	Pyrite	19.2	-	-	-	-	-
SF-14	Paleospring	Drusy quartz vein infill	-	-3.2	-	-	-18.5	-10.0
SF-14	Paleospring	White massive carbonate infill (cal2)	-	-5.0	-21.9	-	-17.5	-10.6
SF-15	Paleospring	White massive carbonate infill (cal2)	-	-0.3	-20.6	-	-12.8	-5.9
SF-17	Paleospring	White massive carbonate infill (cal2)	-	3.2	-23.8	-	-9.4	-2.4
SF-17b	Paleospring	White massive carbonate infill (cal2)	-	0.8	-8.4	-	-11.7	-4.8
SF-14	Paleospring	Orange massive carbonate infill (cal2)	-	1.5	-22.5	-	-11.0	-4.1
SF-10	Paleospring	Brown bladed carbonate lining (cal1)	-	2.1	-29.5	-	-8.0	-1.6
SF-14	Paleospring	Brown bladed carbonate lining (cal1)	-	2.8	-29.2	-	-7.3	-0.9
SF-14	Paleospring	Brown bladed carbonate lining (cal1)	-	1.4	-31.2	-	-8.7	-2.3
SF-15	Paleospring	Brown bladed carbonate lining (cal1)	-	2.6	-30.4	-	-7.5	-1.1
SF-17	Paleospring	Brown bladed carbonate lining (cal1)	-	3.5	-27.3	-	-6.6	-0.2
COC1	Modern spring	Carbonate from modern spring	-	10.0	-10.6	-22.1	-	-

[1]Fractionation equations: calcite-H_2O [140], aragonite-H_2O [141], and quartz-H_2O [142].

rock margins or along host rock-vein contacts are in support of carbonate-sulfide coprecipitation.

5.2.2. Fluid Inclusion Petrography and Microthermometry. Carbonates from representative vein specimens (discrete veins, and "zebra" texture) from the WGVA were examined for fluid inclusions. The vein samples selected for study (e.g., Figures 9(a)–9(c)) contain an early generation of zoned, brown- to tan-coloured, acicular, hexagonal early brown calcite (as cal1) that grew inward from fracture walls to create a symmetrical open-space filling layer on the walls, and a later generation of white to orange massive, polycrystalline to euhedral, terminated "sparry" white-orange calcite (cal2) that infills the central vein cavities lined by terminated crystals of cal1. Quartz is also present, but rare, occurring as a massive, polycrystalline infilling within an even later cavity intergrown with cal2. No differences in the petrographic characteristics (inclusion origins, morphologies) of fluid inclusions from the White Glacier and Striae Hill study areas are observed. The infilling cal2 generation contains primary and secondary inclusions. Both generations of calcite postdate an early generation of base metal sulfide mineralization, with zoned cal1 coating, and infilling fractures within pyrite-marcasite (Figure 9(d)). Trace amounts of secondary galena, pyrite, and sphalerite grew synchronous to, or after, cal2. Primary inclusions in cal2 (Figures 9(e)–9(i)) are rare, up to 80 μm in longest dimension, and have a variety of morphologies, ranging from complex, rectangular to rhombic (Figures 9(f)–9(h)) to long, rectangular (tube-like) in shape (Figure 9(i)). The primary inclusions (type "P") occur in isolated assemblages of up to ~10 inclusions within clear domains of calcite. Secondary inclusions are smaller, and at least two different types are recognized. Type "S" inclusions (up to 30 μm; averaging ~15 μm) (Figures 9(e)–9h, 9(k), and 9(l)) show morphologies ranging from amoeboid, subangular, through rectangular to rhombic, some occurring in planar arrays that cross-cut calcite grain boundaries and cleavage planes. Type "S2" inclusions are less abundant, very small (<4 μm), and have consistently rectangular to rhombic morphologies (Figure 9(m)). The wall-lining cal1 generation contains only irregularly shaped secondary inclusions (Figure 9(n)). In both cal1 and cal2 generations, all inclusion types are two-phase at room T, containing an aqueous liquid (L_{aq}) and a vapour bubble (V), with L : V ratios varying from ~85 : 15 to 90 : 10. Fluid inclusions in the late quartz are too small to investigate (<5 μm, and obscured by a lack of transparency in the quartz) but appear to be two-phase L_{aq} + V.

Table 4 and Figures 10(a)–10(c) summarize microthermometric and calculated salinity data for inclusions in representative secondary fluid inclusion assemblages (FIA) within cal1 and primary and secondary assemblages within cal2. A total of 120 fluid inclusions were measured. In some FIA, only partial microthermometric data could be obtained owing to difficulties in accurately observing ice melting or final homogenization. Primary fluid inclusions show final ice melting (T_m^{ice}; $n = 25$ from two sites) between -7.2°C and -16.8°C, corresponding to bulk salinity between 10.7 and 20.1 wt% NaCl equivalent. Average bulk salinity for primary inclusions is 15.0 wt% $NaCl_{eq}$. Total homogenization (T_h) of primary inclusions occurred by vapour bubble disappearance ($L_{aq} + V \rightarrow L_{aq}$), between 153°C and 293°C (average = 196°C; $n = 12$). Secondary type "S" fluid inclusions show a typically much wider range in final ice melting (T_m^{ice})

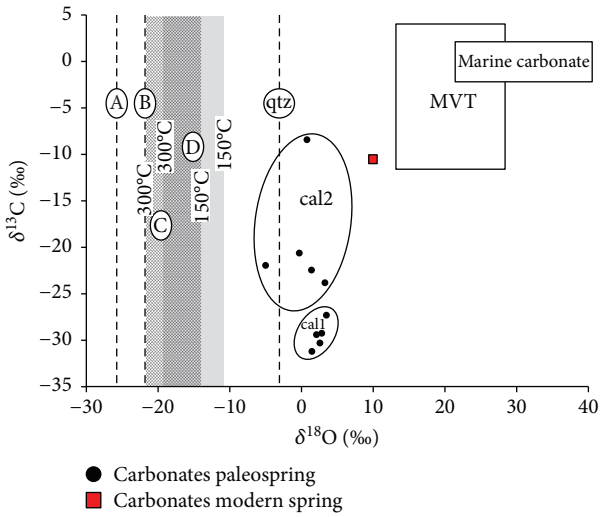

Figure 11: Plot of stable C (‰, relative to VPDB) and O (‰, relative to VSMOW) isotope data for carbonates (cal1 and cal2) from paleospring hydrothermal veins (black circles) and modern carbonate precipitate (red square). Line A is the O isotope composition of meteoric water in the study area (constrained using lat-long-elevation data; using the OIPC3.1 calculator, University of Utah). Line B is the composition of water that would be in equilibrium with modern carbonate at the springs at a mean temperature of 6°C. Fields "C" and "D" are the predicted compositional ranges for carbonates and quartz, respectively, expected if the paleospring hydrothermal veins crystallized at T between 150 and 300°C from meteoric water (based on T_h values from fluid inclusions and utilizing fractionation expressions from [140], [calcite-H_2O], [141] [aragonite-H_2O], and [142] [quartz-H_2O]).

between 0°C and -16.9°C, corresponding to bulk salinity from 0 to 19.8 wt% NaCl equivalent. However, high-salinity secondary inclusions are rare, and the average salinity for secondary inclusions is much lower (3.7 wt% $NaCl_{eq}$; n = 91). The range in T_h for secondary inclusions is similar to that for primary inclusions, between 112°C and 308°C (average = 203°C; n = 73). Overall, there are no discernable differences in salinity or T_h data between secondary inclusions in cal1 or cal2. This, combined with the near complete lack of very high-salinity secondary inclusions in cal1 (as is typical of primary inclusions in cal2), suggests that secondary inclusions in cal1 and cal2 contain the same fluids. Figure 10(a) (n = 10 primary, 68 secondary) shows no correlation between T_h salinity data but illustrates a continuum of inclusion salinities from primary inclusions with consistently highest salinities, through a wide range in secondary inclusion salinity approaching and including ~ pure water. There is relatively little intra-FIA variability in inclusion salinity with only a small number of FIA showing anomalously high- or low-salinity inclusions (Figure 10(b)); given the range in inter-FIA salinity observed in secondary inclusions, anomalously high- or low-salinity inclusions within single assemblages may reflect incorrect assignment for some inclusions within larger groups to a given FIA. Compared to the salinity data, T_h data (Figure 10(c)) shows consistently large intra-FIA variability, up to a ~150°C variation in single FIA. It was noted that stretching of inclusions during heating experiments had a negligible effect on T_h; repeated heating experiments on single inclusions showed no more than a ~1°C increase in T_h even after holding T above T_h for 1 hour before repeat measurements. Petrographic scrutiny of inclusions before microthermometry was performed to exclude any inclusions showing obvious evidence of necking down. However, in the absence of any detectable visual evidence for post-entrapment modification, the effect of inclusion leakage and necking down remains likely given the range in T_h in some FIA. Variability in T_h must therefore reflect post-entrapment leakage or necking down (that could not be detected optically) or real variations in trapping conditions (T or P).

Sparry white calcite contains high-salinity primary inclusion assemblages with individual inclusion salinities ranging from 10.8 to 20 wt% NaCl and T_h values between 153°C and 263°C. Secondary inclusion groups show a wider variation in salinity from 15.6 wt% to as low as ~0 wt% $NaCl_{eq}$ (within measurement uncertainty of ±0.2°C, equivalent to salinity uncertainty of <0.2 wt% $NaCl_{eq}$.) and T_h values between 112°C and 251°C. Importantly, the transition to lower salinities from primary to secondary inclusions suggests overall dilution with time, though fluctuations in salinity during secondary inclusion entrapment appear large (i.e., Figure 10(c), secondary inclusions in cal1 and cal2).

5.2.3. Stable Isotopes. Oxygen and carbon isotope values in carbonate generation cal1 (Table 5, Figure 11) range from +1.4‰ to +3.5‰ ($\delta^{18}O_{VSMOW}$) and -22.5‰ to -31.2‰ ($\delta^{13}C_{VPDB}$), respectively. These data are similar to that for cal2 ($\delta^{18}O_{VSMOW}$ = −0.3‰ to +3.2‰, and $\delta^{13}C_{VPDB}$ = −8.4 ‰ to -23.8‰). Drusy quartz coeval with cal2 has $\delta^{18}O_{VSMOW}$ = −3.2‰. In comparison, the modern (active) spring carbonate has significantly higher isotope ratios ($\delta^{18}O_{VSMOW}$ = +10.0‰ and $\delta^{13}C_{VPDB}$ = −10.6‰). The isotope composition of the modern spring carbonate lies close to the compositional range for post-mineralization pore- and fracture-filling calcite in MVT deposits in the Canadian Arctic (Figure 11; [74, 75]). With respect to O isotopes, at a T = 6°C (mean annual spring discharge T), we calculate a value of $\delta^{18}O_{VSMOW}$ = −22.1‰ (line "B" in Figure 11) for the aqueous solution in equilibrium with the carbonate, slightly higher than the composition of high-latitude meteoric water (i.e., melt water) for the study area (-26‰; OIPC3.1 calculator, University of Utah; line "B" in Figure 11). Over a temperature range from 150 to 300°C (based on primary fluid inclusion T_h) and using a meteoric water composition of $\delta^{18}O_{VSMOW}$ = −26‰ (negligible change in study area latitude beginning in the Eocene-Miocene when the paleosprings at WGVA are assumed to have been active), calculated values of $\delta^{18}O_{VSMOW}$ the carbonate and quartz expected to precipitate from that water range from -22‰ to -14‰ and -19.5‰ to -11‰, respectively (fields "C" and "D" in Figure 11). Note that these ranges represent maximum values since T_h values are minimum fluid inclusion (host mineral precipitation) T_s minimum fluid inclusion entrapment temperatures. Importantly, these values are *at least* ~6‰ lower than the measured mineral

compositions. Estimated $\delta^{18}O_{VSMOW}$ values for fluid in equilibrium with cal2 are lower than for cal1 (Table 5) assuming cal1 precipitated at a similar or higher T than cal2. Consistent with the fluid inclusion salinity data, these results suggest that the hydrothermal minerals did not precipitate from heated meteoric water but rather from a *mixture* of meteoric water and a saline fluid phase, with a larger proportion of meteoric water in the mixture at the time of precipitation of the late carbonate-quartz infilling. Thus, while modern springs show a predominance of meteoric water, the paleosprings formed from mixtures of meteoric water and basinal-type brine, with fluctuations from a dominant brine to dominant meteoric water influence with time. This transition is consistent with fluid inclusion data, showing decreasing salinity from primary to secondary inclusions, approaching ~pure water in many inclusion assemblages.

The strongly depleted nature of carbon isotopes for the WGVA vein carbonates ($\delta^{13}C_{VPDB}$ in cal1 ranges from -22.5‰ to -31.2‰, and that in cal2 ranges from -8.4‰ to -23.8‰) likely reflects a dissolved carbonate source related to oxidation or thermal degradation of organic matter. A shift to higher $\delta^{13}C_{VPDB}$ values from cal1 to cal2 is observed, consistent with the shift from higher to lower values of calculated $\delta^{18}O_{VSMOW}$ for the fluid, resulting from a combination of progressive dilution by meteoric water and/or decreasing equilibration T.

Values of $\delta^{34}S_{VCDT}$ in pyrite(-marcasite) in the vein margins of the WGVA are variable (-2.7 to +16.4‰) with the highest value approaching that for Carboniferous-age evaporite diapir sulfate [76]. The wide range in $\delta^{34}S_{VCDT}$, combined with textural evidence for recrystallization of pyrite framboids, and likely thermal and compositional fluctuations in the hydrothermal system with time suggest that S isotope systematics of the WGVA reflect a combination of preserved low-temperature microbial sulfate reduction and higher-temperature reduction of sulfate by organic compounds (*c.f.* in MVT systems; [77]).

6. Discussion

6.1. Justification for an Alternative Model. The surficial model by Andersen et al. [7], which envisaged recharge from glacial lakes and near-surface circulation through evaporites and permafrost (see Section 4), was justifiable with the data available, but the younger thermal history detected by thermochronology suggested that the PSS phenomenon might have a deeper, internal energy connection. The apatite fission track dating method (Figure 4) constrains not the age, but the geological time when rocks cooled for the last time below ca. 100°C (corresponding to a depth of 3 to 4 km under normal geothermal gradients) and allows for modelling compatible time-temperature histories (e.g., [78]). Regionally, rocks now exposed at the surface cooled to temperatures below 100°C during uplift and exhumation due to the rise of mountains on Axel Heiberg Island and Ellesmere Island (Figures 4(a) and 4(b)) between ca. 62 and 33 Ma (Paleogene; [79]) caused by tectonic collision with Greenland (e.g., [5, 80]). In contrast, rocks in the Expedition Fiord area of Axel Heiberg Island (Figure 4(c)) cooled 10 to 20 My later [9, 81].

Two samples are clearly anomalous (Figure 4(a)): (1) sample SF-66, collected at the surface of the Cretaceous age gabbro Wolf Intrusion (Figure 2) between Colour Peak Diapir and White Glacier, and (2) sample SF-59, collected in a raft of gabbro intrusive within the Colour Peak Diapir (Figure 2). Their apatite fission track ages are younger than most regional samples, and their mean track length is the shortest measured in surface rocks in this area (Figure 4(a); Table 1). These characteristics suggest that, relative to other rocks, they remained within the crust for a longer time at a higher temperature. Figures 4(b) and 4(c) depict the result of Monte Carlo inverse thermal history models for two representative samples, including that from the Wolf Intrusion (SF-66) and another (SF-28) from near the summit of the Princess Margaret Range, ca. 60 km to the northeast (79.7°N; 88.5°W; 2467 m.a.s.l.). Both internally consistent cooling models used the AFTINV annealing model [48, 82, 83]. The model in Figure 4(c) is compatible with the interpretation that the rocks now at the surface in the region of the Wolf Intrusion (sample SF-66, Figure 2) could have maintained temperatures of up to ca. 75°C until the Miocene (ca. 15 Ma) and cooled since. Acceptable model solutions involving heating at higher temperatures for shorter time periods may also be compatible with the data (Figure 4(c)).

6.2. Comparison of PSS and WGVA. The active PSS in Expedition Fiord and the high-temperature veins in WGVA have many geological similarities that suggest a kinship, calling for a modification of the previous interpretations that the PSS are merely recent periglacial phenomena (e.g., [7, 50]).

6.2.1. Location. The PSS are in proximity (marginal) to anhydrite-gypsum diapiric structures, in zones that are characterized by faulting and brecciation. They are close to sea level or at the level of local rivers. The WGVA are not so close (~1-3 km) to mapped evaporite diapirs (Figure 2), but the brecciated evaporitic host rocks exposed and the proximity to large faults, which are probably rooted in diapirs at depth as suggested by geological cross sections by Jackson and Harrison [84], make it likely that a portion of their postulated evaporite salt canopy structure exists in the subsurface.

6.2.2. Size. The exposed plumbing systems (Figure 3) are comparable in areal size: PSS at Colour Peak Diapir and Gypsum Hill Diapir are 250×200 m and 400×50 m, respectively, but it is probable that they extend underneath Expedition Fiord and the Expedition River valley. The WGVA has exposures of more than 300×50 m but also extends under the glacier. Its visible vertical extent is 100 m or more; an unknown volume has been eroded.

6.2.3. Structures and Textures. The plumbing system at the WGVA consists of predominantly vertical, vein-like conduits lined by radial aggregates; however, both the WGVA and the PSS at Colour Peak Diapir exhibit banding, cyclic laminae at the mm scale in the PSS and mm to cm scale in the WGVA. The WGVA veins are crustified, often symmetrical, with acicular or fibrous crystals growing perpendicular to the margins, and some have large sparry (clear) crystals in the centre. The cyclicity in both implies the action of recurring pulses of

mineral-laden fluids, which is the likely cause for laminated fabrics in the PSS mineral precipitates at Colour Peak Diapir. Sulfides occur in the WGVA within microfractures in the host rocks and as botryoidal aggregates in former open spaces up to decimetre scale.

6.2.4. Mineralogy. Both systems are mineralogically similar. The predominant mineral in both the PSS at Colour Peak Diapir and the WGVA is calcium carbonate in the form of calcite; laminated fabrics at Colour Peak Diapir contain mixtures of carbonate and micritic laminae with organic matter [55] and metal enrichments in Fe, Mn, Zn, Cu, and Ni. In addition to a predominance of calcite ($CaCO_3$), other phases identified in the PSS are halite (NaCl), ikaite ($CaCO_3{\cdot}6H_2O$), gypsum ($CaSO_4{\cdot}2H_2O$), thenardite (Na_2SO_4), mirabilite ($Na_2SO_4{\cdot}10H_2O$), and elemental sulfur (S°), which form in association with spring discharge [55–57]. The calcite in the WGVA shows signs of recrystallization judging from its mineral habit (orthorhombic blades and pseudo-hexagonal prisms resulting from twinning); therefore, it probably crystallized originally as aragonite. The pseudomorphs, however, yield calcite Raman spectra. Sulphates are also present as anhydrite ($CaSO_4$), gypsum, and barite ($BaSO_4$) but in the host breccias, not in the veins. The Fe- and Mg-rich mafic igneous host rocks of the WGVA contain epidote and chlorite as alteration of magmatic silicates, and the bulk of the Fe sulfides (marcasite and pyrite) occur within or near the mafic rocks, suggesting that they supplied the iron. However, the "zebra" banded carbonates rich in organic matter contain sulfides in the form of framboids and botryoidal aggregates. Sulfide (pyrite) microcrystalline aggregates similar to framboids are also observed within the banded mineral precipitates of the PSS at Colour Peak Diapir (Figure 5); the presence of hydrogen sulfide in discharging waters suggests microbial sulfate reduction, which is confirmed by sulfur isotope data of micritic sediments (see below). Chalcopyrite, sphalerite, galena, pyrrhotite, and arsenopyrite have so far been observed only in the WGVA and especially in the proximity of mafic igneous rocks.

6.2.5. Fluid Chemistry. A direct comparison of the chemistry of the rocks in the PSS and WGVA is not possible because the sampling and methodologies utilized were different. However, the fluids within the former can be compared with the inclusion fluids in the latter. The salinity of the brines in the PSS is bimodal, some yielding relatively low salinity fluids between 8 and 9% and others higher-salinity fluids of 16-17%; similarly, there is evidence for two different types of fluids in the fluid inclusions in the WGVA, 1.5% and 16% NaCl equivalent. The inclusion data in the WGVA suggest a progressive dilution with time from a ~20 wt% NaCl brine end-member down to ~pure (meteoric) water with evidence of large variability in salinity during progressive trapping of secondary inclusions. In comparison, the modern springs in the PSS show a variability in salinity from location to location from ~4.7 to 18.9 wt% NaCl equivalent [57] supporting the kinship between both systems. In both systems, chlorine is the most abundant halogen, and Ca and Na are the most abundant alkalis, reflecting the spatial association with evaporites, also manifest by the presence of sulfate. More internally consistent work needs to be done to confirm the comparisons made here.

6.2.6. Metals. Iron is the predominant metal sulfide in both systems, with 35 to 100 ppm sulfide (presumably as Fe sulfide) in the PSS precipitates [57], although the surfacing brines are not enriched in Fe (2 ppm; [60, 63]). In the WGVA, the sulfide content is extremely variable, from traces to 100%. The geochemical analyses of heavy mineral concentrates contain 32% Fe, 0.2% Mn, and small amounts of Ag (0.2 ppm), Cu (9 ppm), Pb (3 ppm), Zn (13 ppm), and Ba (430 ppm). These values are like those detected in 3 rock samples from a gossan in a raft of diabase adjacent to the PSS Colour Peak Diapir.

6.2.7. Stable Isotopes. Oxygen isotopes: the $\delta^{18}O_{VSMOW}$ value of the PSS hypersaline fluids is +10‰, thus dominantly high-latitude meteoric water but with a very minor non-meteoric (brine) component. Recalculation of the water composition that would be in equilibrium with the perennial spring carbonate at ~6°C (Figure 11, Table 5) gives a $\delta^{18}O_{VSMOW}$ value of -22.1‰ (similar to -26‰ for modern meteoric water in the study area; constrained using lat-long-elevation data using the OIPC3.1 calculator, University of Utah) suggesting a greater meteoric water contribution to the existing spring carbonates than in the current circulating fluid. The $\delta^{18}O_{VSMOW}$ values in the early brown (cal1) and later (cal2) carbonates at the WGVA range from -0.3‰ to +3.5‰, which based on fluid inclusion minimum trapping temperatures (~150-300°C), constrain minimum $\delta^{18}O_{VSMOW}$ values for coeval fluid between -0.2‰ and -8.7‰. This range in fluid $\delta^{18}O_{VSMOW}$ is explained through mixing of high-latitude meteoric water and a heated saline formational water or basinal brine.

Sulfur isotopes: ($\delta^{34}S_{VCDT}$) in the PSS at Colour Peak Diapir is +19.2‰ (sulfide separated from laminated carbonate-organic matter deposits) consistent with microbial sulfate reduction. In the WGVA, they range from -2.7‰ to +16.4‰, having a more ambiguous origin but likely preserving either low-temperature microbial sulfate reduction or higher-temperature reduction of sulfate by organics. The sulfur isotope systematics may have been somewhat altered by surface weathering, and more research is needed to confirm that the range in values for sulfides from the WGVA are not modified.

Carbon isotopes: $\delta^{13}C_{VPDB}$ in the PSS-laminated carbonate at Colour Peak Diapir is -10‰, suggesting an organic carbon component reflected in the measured isotope composition. The $\delta^{13}C_{VPDB}$ values in carbonates in the WGVA are -20.6 to -31.2‰, compatible with an origin from degradation of petroleum at depth. Specifically, the highly negative $\delta^{13}C_{VPDB}$ values associated with early cal1 are consistent with sourcing of hydrothermal carbonate from fluids that oxidized organic matter. Increasing $\delta^{13}C_{VPDB}$ with time approaches the same value as the PSS carbonate and nearer to the compositional field for post-ore carbonates filling pore spaces in host rocks from major MVT deposits in the Arctic of Canada [74, 75].

6.2.8. Temperature. As indicated above, the temperature of the PSS at Colour Peak Diapir is rather invariable at ~6°C [55]. The fluid inclusions in the WGVA indicate that the fluids had temperatures from 100°C to 300°C (Figures 10(a) and 10(b)). This higher temperature is compatible with the presence of epidote adjacent to the veins, requiring temperatures between ~200°C and 350°C to crystallize from hydrothermal fluids [85, 86]. It is unclear whether the fluids at depth in the PSS have warm temperatures and equilibrate with the surrounding permafrost to result in a temperature of ca. 6°C as suggested by Andersen et al. [7] or if they presently circulate to greater depths, as they must have done in the past to account for the fluid inclusion data. The inclusion data do not portray any correlation between T_h and salinity across the large continuous range in salinity observed. This can be interpreted in 2 ways: (a) maintenance of fluid T (i.e., between approximately 150°C and 250°C) during progressive dilution (unlikely because it would require the low-salinity fluid to be heated before mixing) or (b) a cooling trend from early high salinity to low salinity, if P decreased from quasi-lithostatic to hydrostatic conditions (i.e., if we correct T_h for P); exhumation of the system may have contributed to this transition. This second explanation agrees with stable isotope data (showing increasing amounts of likely meteoric water requiring a more open system to allow incursion and mixing).

6.3. Framboidal Pyrite. Framboidal pyrite has been observed in the WGVA (Figures 9(f) and 9(g)), and Fe-sulfide microlite-like constituents of framboids are observed in micritic layers in banded carbonate in the PSS at Colour Peak Diapir (Figure 5). The origin of framboidal pyrite has been debated since first described from ores in sedimentary strata by Schneiderhöhn [87] who described them as "mineralized bacteria," although subsequent research demonstrated that they can form in purely inorganic systems. Nevertheless, experimental work shows they generally form at temperatures below 100°C in environments where bacteria are present. Wilson et al. [88] argued for bacterial growth of framboids within liquid petroleum at depths of several km, based on textural evidence and sulfur isotopes, and recently Lin et al. [89] demonstrated that framboids can grow rapidly where anaerobic oxidation of methane is coupled with microbial sulfate reduction. The spherical shape of framboid aggregates has been ascribed to colloidal phenomena, or to the replacement of minute vacuoles, but their formation has proven extremely difficult in the absence of organic matter [90]. The presence of organic matter enhances the chemical formation of pyrite combining metals and biologically produced hydrogen sulfide [90]. Wilkin and Barnes [91] explain the growth of framboids in four consecutive stages: (1) nucleation and growth of initial iron monosulfide microcrystals, (2) reaction of the microcrystals to greigite (Fe_3S_4) or mackinawite (Fe_9S_8), (3) aggregation of uniformly sized greigite microcrystals, i.e., framboid growth, and (4) replacement of greigite framboids by pyrite or marcasite. Some of the microcrystalline Fe-sulfide textures observed in the PSS at Colour Peak Diapir (Figure 5(k)) illustrate this sulfide evolution. Vietti et al. [92] found that framboids grew readily within sulfidic microbial biofilms by bacterial degradation of organic matter. If there is continued influx of Fe, the originally spheroidal aggregates of microlites progressively recrystallize into idiomorphic (cubic or octahedral) crystals; this recrystallization is prevented if the framboids are isolated from new input of Fe, as within a biofilm, petroleum, or an enclosing mineral [93, 94]. Pyrite framboids formed during catastrophic dysoxic events in sedimentary basins [95] and in methane seeps associated with gypsum, where biogenic activity is possible [89]. Despite controversy, some authors are persuaded that pyrite framboids are associated with bacterial activity (e.g., [96, 97]). Both low-grade metamorphism and fluid-rich diagenesis can lead to framboid recrystallization and formation of aggregates with framboidal cores and euhedral edges [98]. Heating above 150°C makes marcasite revert to pyrite [49, 99, 100].

The presence of pyrite with microlites similar to those in framboids in the PSS at Colour Peak Diapir is a possible sign of anoxic reduction during the flow of hydrocarbons (methane) and/or microbial activity, which would explain the preliminary sulfur isotope signature. The presence of framboidal pyrite in the WGVA is suggestive of interaction with hydrocarbons at depth but also of microbial activity when marcasite was also the stable phase of Fe sulfide, probably at temperatures below 100°C. The evidence for recrystallization of framboids and the reversion of marcasite to pyrite indicate subsequent heating.

6.4. "Zebra" Textures. The "zebra"-textured veins at WGVA (Figures 7(e)–7(g)) were formed by "open space filling" and have similar mineralogy and texture to subvertical veins in the area, within diabase or brecciated sedimentary rocks. The term "zebra" texture has been applied to arrays of subparallel veins in base metal ore deposits or dolomitized carbonate masses, where there is light and dark banding that reminds of a zebra coat. They have bilateral symmetry about a central mineral band (C) with repetition of sulfide and/or gangue mineralogy in the following form: A B C B A, where A, B, and C represent different mineral phases or different generations of a single mineral phase (*c.f.* [101–103]). Originally, sedimentological and diagenetic evidence led early authors to describe their formation immediately below the sediment-water interface as "diagenetic crystallization rhythmites." However, the early-diagenetic interpretation has been rejected as a general model, since various types of zebra veins have been described in various geological environments. For instance, in the Nanisivik Pb-Zn-Ag deposit located on northwest Baffin Island (lower right in Figure 1), zebra vein arrays very similar to those at WGVA were interpreted to have formed by pulses of basinal fluids, later than lithification of the host sediments at temperatures more than 200°C [104, 105]. Recent workers (e.g., [106]) interpret zebra veins in a Mississippi Valley Type base metal deposit in the Andes as having formed as sheet cavity networks developed by extensional fracturing in deep subsurface environments such as the filling of subhorizontal tension fractures formed during thrusting. Under these conditions, the most effective mechanism to generate subparallel tension fractures is fluid overpressure and episodic hydraulic fracturing (e.g., [107–109]),

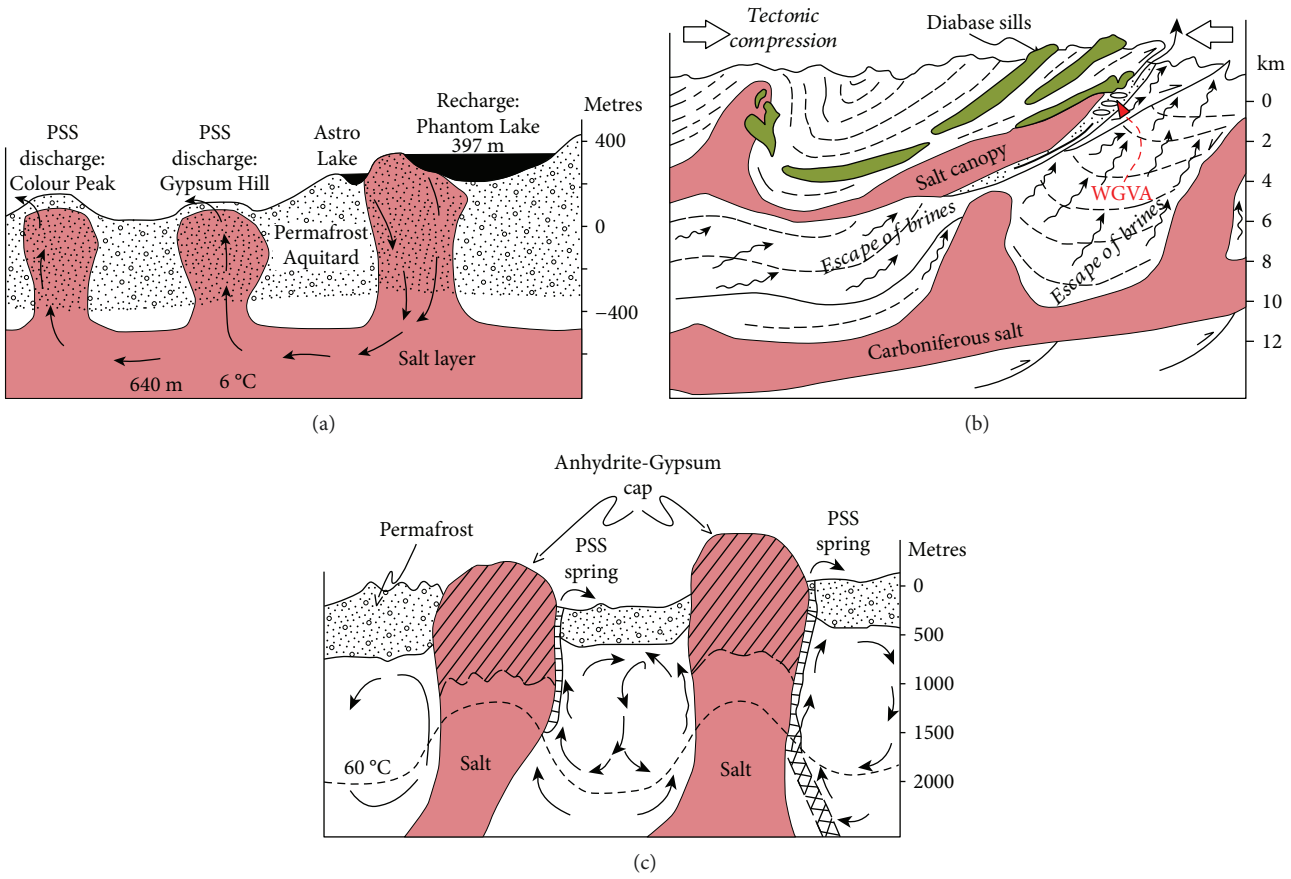

Figure 12: (a) Model for the perennial springs (PSS) as first published by Andersen et al. [7] with fluid recharge from glacial lakes through permeable evaporite (salt) diapirs, shallow circulation, and continuous escape. (b) Proposed model for White Glacier vein array (WGVA). Overpressured hot basinal fluids expelled episodically through faults from under the salt canopy during tectonic compression of the Eurekan Orogeny (hypothetical subsurface structure modified from [6]). (c) Proposed hypothetical model for the perennial springs, where fluids have a mixed origin and escape marginally to evaporite (salt-anhydrite-gypsum) diapirs through plumbing systems established during tectonic deformation (b). Not to scale. See text for discussion including description of lithologies.

repeated cycles of hydraulic fracturing and healing like the mechanism responsible for banded veins referred to as "crack-seal" veins (e.g., [110]). The generation of episodic basin dewatering of overpressured fluids in sedimentary basins with evaporites is a common phenomenon, especially if enhanced by compressive tectonics [111–113], but also due to rapid compaction [114] and in the environment of salt dome cap rocks [115]. Finally, Warren [69] discusses the common development of geopressured fluids in the environment of salt canopies similar to the one underlying Expedition Fiord as defined by Jackson and Harrison [6]. An alternative hypothesis for the formation of zebra textures relates them to force of crystallization during diagenesis or mineral replacement (e.g., [102, 116]), but we consider these interpretations not applicable to the WGVA.

Similar "zebra" textures in the PSS at Colour Peak Diapir (Figure 5(b)) at a millimeter scale were formed by a different process, since they are obviously formed at or near the surface by successive pulses of expelled fluid. It is likely that at depth in the PSS (and analogous WGVA) the conduits are lined with similarly banded, crustified mineral coatings. Drilling will be necessary to better understand their nature.

6.5. Towards a Deeply Circulating Model for the PSS. The similarities between the PSS and WGVA make it likely that both systems have some genetic kinship. Pollard et al. [3] considered it unlikely that meteoric or surface water could be the source of the brines in the PSS, yet the hypothetical model by Andersen et al. [7, 50, 66] (Figure 12(a)) envisaged relatively surficial circulation of fluids, with recharge from Astro and Phantom Lakes, which are located on the eastern flank of Thompson Glacier, ~397 m above the outlet of the springs (upper right corner of Figure 2). Andersen et al. [7] assumed (Figure 12(a)) that the deep subsurface salt layer acts as a "reservoir and conduit" of water. Seasonally, the lakes drain partially (1-2%) and the water would circulate to the PSS through faults, such as the ones mapped in the area (Figure 2). Water would flow below the surface at a depth of 600 to 700 m via an evaporite layer, returning to the surface through the piercement structures associated with the springs. Below the surface, the water would attain the geothermal temperature (they assumed a geothermal gradient of 37.3°C/km after [54]). As they flow upward, the brines would lose heat to the surrounding permafrost.

The Andersen et al. [7, 50, 66] model is problematic. Firstly, evaporites (salt, anhydrite, and gypsum) in the near-

surface are among the most impermeable rocks in nature. Powers et al. [117] and Holt and Powers [118] have argued that it is virtually impossible for meteoric water to penetrate evaporitic rocks; under similar conditions in salt (halite), water would take 3 to 30 million years to advance 1 m, in anhydrite 300,000 years [119]. Even in active salt springs around salt diapirs in semi-desert Iran, Zarei and Raeisi [120] assume that surface recharge cannot penetrate more than 10 m. A further problem is that if halite is present, it is difficult to maintain permeability, because porosity becomes occluded [121]. Peripheral fracturing can lead to focussed fluid flow (e.g., [69]), but the geological map and cross sections (Figure 2; [6, 27]) show that there is no likely shallow continuous body of evaporite between Astro Lake and Colour Peak Diapir, a distance of ~20 km. More likely evaporites act as impervious barriers, and any circulation would be peripheral and focussed by them. The surficial water flow model is unlikely considering the independence of PSS brine flow temperature and wide air temperature variations between winter and summer at this latitude. Evaporite-focussed fluid leakage was postulated by Keen [122] to explain heat flow anomalies above salt diapirs in offshore Nova Scotia. Although salt conducts heat many times more effectively than other sediments, Keen [122] concluded that conduction alone could not explain the anomaly, and advective heat from escaping warm fluids was required; for the model, she assumed that the aquifer temperature would be 150°C, hence definitely did not consider surficial seawater. Evans et al. [123] have explained the mechanisms responsible for advection of fluids near salt domes, and Warren [69] discusses the flow of warm brines peripheral to evaporite diapir regions where salt canopies have developed. In the Expedition Fiord area, the evidence is compatible with models in which the PSS fluids migrate upward from considerable depth following previously developed plumbing systems marginal to evaporite bodies (Figure 12(c)), either by vein arrays such as those at WGVA or brecciation typical of the margins of displaced allochthonous salt masses [69]. The involvement of hydrocarbons in the reactions leading to precipitation of minerals including carbonates and sulfides in the above systems further suggests a connection with petroleum seeps, difficult to ascribe to surface recharge, especially in a polar region with thick permafrost. Liquid and gaseous hydrocarbons are present in fluid inclusions (Zentilli, unpublished data) in the Colour Peak Diapir (Figure 1), and deep wells drilled on salt-cored anticlines indicate the presence of adequate source rocks [21].

The apatite fission track data suggest that the rocks now at the surface in Axel Heiberg Island outside the area of the WGVA were at temperatures of ca. 100°C in the Eocene (Figure 4(b) and [8]). Based on industrial thermal data (156 deep wells) and coalification gradients, during the Paleogene the geothermal gradient in this region is estimated to have been 28 ± 9 mK/m [124], which translates into 2.7 to 5.3 km (avge. 3.6 km) of erosion. Since in the area of the PSS and WGVA the thermal regime was anomalous due to fluid advection, it is problematic to be certain of its paleogeothermal gradient. However, the apatite FT models are compatible with rocks now at the surface having been at temperatures of ca. 75°C (with large uncertainty, Figure 4(c)) until the Miocene, and one can estimate between of 0.5-2 km of exhumation until the veins were exposed by glacial erosion. The WGVA is located near the bottom bedrock of the White Glacier valley; hence, much of the mineralized zone may have been eroded. It is problematic to assess how much pre-glacial erosion has taken place in the Expedition Fiord area. When mountains in Axel Heiberg Island were rising in the Eocene, the climate was warm and humid, leading to the formation of forests (e.g., [10]), and it is unlikely that large glaciers occupied the region through the Miocene, so ensuing erosion was probably due to fluvial incision and exhumation related to landsliding of steep slopes (John Gosse, personal communication). The Late Miocene through Pliocene appears to have been a time of net deposition in the Canadian Arctic, resulting in the infilling of preexisting valleys or grabens, and extensive depositional surfaces until 2.7 Ma [125–127]. Those surfaces were subsequently incised, perhaps initially by streams, but more significantly by warm-based outlet glaciers [128] and independent valley glacier systems. While erosion by valley and outlet glaciers through unconsolidated sediment is likely to have been rapid, even bedrock has been incised by more than 80 m/Myr [129] to form fiords. However, under cold-based glaciers which occupied many summit plateaus in Arctic Canada, subglacial erosion can be negligible, as indicated by the survival of moss under cold-based glaciers for more than 5 ka [130, 131].

The fluid inclusions indicate the carbonate and sulfide minerals in the veins crystallized from more than one pulse of hot fluids with temperatures between 100°C and 300°C, and strong swings in pressure can be ascertained. The veins and zebra textures were formed in open spaces, which at a depth of a few km could only have been present if the fluids were at lithostatic pressure plus the tensional strength of the rocks [107]. The environment in which the WGVA developed is one of evolving allochthonous evaporite, with a large salt canopy at depth [6]. The region underwent strong compression during the Paleogene Eurekan Orogeny (Figure 12(b)). The zebra textures described at the WGVA are like zebra textures developed in compressive tectonic environments associated with thrusting in fluid overpressured zones (e.g., [106]). The host rocks of the WGVA are fractured mafic igneous rocks physically intermixed with a breccia or conglomerate that has some similarities with "gumbo" found in association with displaced allochthonous salt masses in various basins rich in evaporites in Oman, the Gulf of Mexico, offshore Angola and Brazil; these brecciated rocks are characteristically strongly overpressured when intersected by drilling [69].

Although overpressures may develop under autochthonous and evolving allochthonous layers of salt by simple compaction [132, 133], in some instances it leads to the generation of metallic ore deposits [114]; compressional tectonics can intensify them (Oliver, 1986; [112]). The Eurekan Orogeny (Paleogene) in the Sverdrup Basin resulted from collision of Greenland with the Canadian Arctic Archipelago [134] and led to the formation of high mountains (Figure 1) by stacking. Most thrust faults are rooted in salt, and a

particular case is the formation of the folded wall-and-basin structure province that underlies Expedition Fiord, caused by shortening during the Eurekan Orogeny.

We suggest (Figure 12(b)) that during the Eurekan Orogeny, overpressures were generated under the shifting salt canopy of Jackson and Harrison [6], and successive pulses of hot fluids were expelled, which developed, by hydraulic fracturing, the veins and subparallel zebra rocks of the WGVA in a local tensional (dilatant) environment. It is a characteristic of overpressuring in this environment to reach a point where the effective pressure overtakes the lithostatic pressure and tensional strength of the rocks [107], and a fracture (and a "fracking" earthquake) ensues. Once sufficient volume has been created (dilation) to accommodate the fluid or let it escape, the fluid pressure drops. However, localized pressure drop has little effect on the first-order cause of the tectonic compression, so the pressure builds up again until a new "fracking" event occurs. A sudden pressure drop, combined with decreasing fluid salinity and temperature resulting from mixing of brine and meteoric water, is an optimal mechanism to reduce aqueous CO_2 solubility [135, 136]. These processes would precipitate carbonate on the walls of the recently created cavities and fractures followed by quartz precipitates forming the later cavity infilling textures (after carbonate) observed in the veins. However, fluid inclusion observations do not support boiling/CO_2 unmixing as a process that took place in the veins. Thus, while pressure fluctuations sufficient to cause fracture formation are mandatory, these pressure fluctuations were not sufficient enough to cause boiling/unmixing. Fluid mixing and cooling were likely important for vein mineral precipitation.

The fluids expelled from the overpressured zones contain small amounts of Cu, Zn, and Pb, which are typical in Mississippi Valley Type (MVT) deposits associated with salt diapirs [115, 137]. The precipitation as sulfides requires the presence of sulfur as dissolved sulfate from the evaporites, and some reduction mechanism to generate hydrogen sulfide. An ideal redox reaction would be the oxidation of organic matter that would be resident in porous sedimentary rocks as petroleum (oil or gas) and the concomitant reduction of dissolved sulfate. Microbial reduction could be a contributing factor, and probably was. The base metal sulfides are generally in veins marginal to the larger carbonate veins, very often in the mafic igneous rocks. The presence of pyrite-marcasite seems to coincide with the presence of mafic igneous rocks rich in Fe (magnetic when fresh). Hence, it is possible that some of the base metals are extracted from the altered diabase and that oxidation of magnetite is accompanied by reduction of sulfate. The fluid expulsion phenomenon was of regional proportions, and if it led to the formation of the WGVA, it is likely to have formed other similar mineralized sites, and this possibility seems confirmed by the presence of gossans in the vicinity of many diapirs in Axel Heiberg Island (e.g., [138]).

The kinship between the WGVA and the modern PSS is further supported by the fluid inclusion data, which suggest a progressive dilution with time from a ~20 wt% NaCl brine down to ~pure water, with a spread of data right across this range. Therefore, we propose that the PSS are exploiting a plumbing system established during the formation of the WGVA (Figure 12(c)).

7. Conclusions

(1) A carbonate vein array with metal sulfides recognized on the western boundary of White Glacier (WGVA) is interpreted to be the remnants of a hydrothermal system developed during the Eurekan Orogeny. Hydraulic fracturing by overpressured fluids led to brecciation of rocks and formation of carbonate veins in dilatant zones peripheral to allochthonous evaporite masses; brecciation of the host rocks may have developed earlier, during displacement of the salt canopies and diapirs (see Section 5.2). Processes envisaged are similar to those leading to the genesis of base metal deposits know as Mississippi Valley Type (MVT) deposits.

(2) Initially, the WGVA was formed by hot fluids with a minimum temperature of 150°C to 300°C and having high salinity, in successive pulses with wild pressure changes related to hydraulic fracturing, and later was invaded by dilute fluids of lower temperatures. The depth of emplacement can be estimated to have been a minimum of 0.5 km.

(3) The pervasive advection of hot fluids in the Expedition Fiord region explains the anomaly detected by apatite fission track thermochronology which suggested that the rocks now at the surface cooled below 100°C in the Miocene, ca. 20 My later than similar rocks regionally in Axel Heiberg Island and Ellesmere Island. Hydrothermal activity initiated in the Eocene continued for a long time with involvement of cooler, more dilute fluids, extending to this day.

(4) Perennial springs (PSS) on Axel Heiberg Island that discharge waters at constant temperatures irrespective of air temperature in an area with ca. 600 m of permafrost are not surficial, periglacial phenomena as previously interpreted, but are instead related to deep plumbing systems established by expulsion of overpressured fluids from under plastically displacing impermeable salt structures during tectonic, compressive deformation and thrust faulting in the Paleogene Eurekan Orogeny.

(5) Microbial activity and the involvement of hydrocarbons throughout the history of the WGVA is supported by mineralogy and stable isotope data. If this spring activity has lasted for ca. 10 My as suggested, it could have allowed for isolated evolution of microorganisms since the brines cooled sufficiently to permit their survival. Future work, preferably supported by deep drilling both at the WGVA and PSS, will determine the presence and diversity of microorganisms in these deep subsurface environments.

Data Availability

All data discussed in paper are in 4 tables. Any other data available on request.

Conflicts of Interest

The authors declare that they have no conflicts of interest.

Acknowledgments

The authors acknowledge support from the Natural Sciences and Engineering Research Council of Canada (NSERC) through grants to M. Zentilli, J. Hanley, and W. Pollard, and an NSERC PDF to C. Omelon. Additional funding for student research was provided by the Department of Indian and Northern Affairs Northern Scientific Training Program and McGill University's Centre for Climate and Global Change. Field work was supported by the McGill Arctic Research Station (MARS) (c/o Wayne Pollard, without whose support and encouragement this research would have been impossible), the Canadian Space Agency (c/o Gordon Osisnki), the Geological Survey of Canada, and the Polar Continental Shelf Program (c/o Marie-Claude Williamson, Party Chief 2003). We are grateful to Marie-Claude Williamson, with whom the first author first visited the perennial springs, subject of this paper. We thank Alexander (Sandy) Grist for apatite fission-track data and time-temperature modelling, Yawooz Kettanah for fluid inclusion microthermometry from one sample, Dale T. Andersen for stimulating discussions and field photos; John Gosse for advice on the Cenozoic erosion of the study region, Laura Thomson for educating us about glaciers, and Randolph Corney for drafting. We are also grateful to Todd Simpson and Tim Goldhawk of the Western Nanofabrication Facility for technical expertise. This research used resources of the Advanced Photon Source, a U.S. Department of Energy (DOE) Office of Science User Facility operated for the DOE Office of Science by Argonne National Laboratory under Contract No. DE-AC02-06CH11357. Data was collected at the X-Ray Science Division at the Advanced Photon Source, Argonne National Laboratory; we thank the Sector 20 beamline staff for their support of this research.

References

[1] P. T. Doran, C. P. McKay, W. P. Adams, M. C. English, R. A. Wharton, and M. A. Meyer, "Climate forcing and thermal feedback of residual lake-ice covers in the high Arctic," *Limnology and Oceanography*, vol. 41, no. 5, pp. 839–848, 1996.

[2] R. E. Beschel, "Sulphur springs at Gypsum Hill," *Preliminary. report 1961-1962. Axel Heiberg Island Research Report*, McGill University, Montréal, QC, USA, 1963.

[3] W. Pollard, C. Omelon, D. Andersen, and C. McKay, "Perennial spring occurrence in the Expedition Fiord area of western Axel Heiberg Island, Canadian High Arctic," *Canadian Journal of Earth Sciences*, vol. 36, no. 1, pp. 105–120, 1999.

[4] W. H. Pollard, T. Haltigin, L. Whyte et al., "Overview of analogue science activities at the McGill Arctic Research Station, Axel Heiberg Island, Canadian High Arctic," *Planetary and Space Science*, vol. 57, pp. 646–659, 2009.

[5] G. R. Davies and W. W. Nassichuk, "Carboniferous and Permian history of the Sverdrup Basin, Arctic Islands," in *Geology of the Innuitian Orogen and Arctic Platform of Canada and Greenland*, H. P. Trettin, Ed., pp. 345–367, Geological Survey of Canada, Ottawa, Canada, 1991.

[6] M. P. A. Jackson and J. C. Harrison, "An allochthonous salt canopy on Axel Heiberg Island, Sverdrup Basin, Arctic Canada," *Geology*, vol. 34, no. 12, pp. 1045–1048, 2006.

[7] D. T. Andersen, W. H. Pollard, C. P. McKay, and J. Heldmann, "Cold springs in permafrost on Earth and Mars," *Journal of Geophysical Research*, vol. 107, no. E3, 2002.

[8] D. C. Arne, A. M. Grist, M. Zentilli, M. Collins, A. Embry, and T. Gentzis, "Cooling of the Sverdrup Basin during tertiary basin inversion: implications for hydrocarbon exploration," *Basin Research*, vol. 14, no. 2, pp. 183–205, 2002.

[9] M. Zentilli, A. M. Grist, and M.-C. Williamson, "Paleothermal effects of salt diapirs detected by apatite fission track thermochronology," in *Abstracts of the European Conference on Thermochronology, Bremen, Germany*, vol. 49, p. 35, Schriftenreihe der Deutschen Gesellschaft für Geowissenschaften, 2006.

[10] M. Zentilli, A. M. Grist, and M.-C. Williamson, "The Stolz Thrust and its connection with the Eocene Metasequoia Fossil Forest of Axel Heiberg Island, Canadian Arctic Archipelago: Apatite Fission Track Evidence. Abstract," in *Proceedings from the 11th International Conference on Thermochronometry*, pp. 280–282, Anchorage, Alaska, September 2008.

[11] A. V. Okulitch and H. P. Trettin, "Late Cretaceous. Early Tertiary deformation, Arctic Islands," in *Geology of the Innutian Orogen and Arctic Platform of Canada and Greenland*, H. P. Trettin, Ed., pp. 467–489, Geological Survey of Canada, Geology of Canada, No. 3, 1991.

[12] B. D. Ricketts and R. A. Stephenson, "The demise of Sverdrup Basin: Late Cretaceous-Paleogene sequence stratigraphy and forward modeling," *SEPM Journal of Sedimentary Research*, vol. 64B, no. 516, p. 530, 1994.

[13] Department of Energy, Mines and Resources Canada, *The National Atlas of Canada; Natural Resources Canada, Geomatics Canada, MCR Series no. 4177, 1995*, Department of Energy, Mines and Resources Canada, Ottawa, Canada, 1995.

[14] M. J. van der Ploeg, S. Haldorsen, A. Leijnse, and M. Heim, "Subpermafrost groundwater systems: dealing with virtual reality while having virtually no data," *Journal of Hydrology*, vol. 475, pp. 42–52, 2012.

[15] R. Barbieri and N. Stivaletta, "Continental evaporites and the search for evidence of life on Mars," *Geological Journal*, vol. 46, no. 6, pp. 513–524, 2011.

[16] A. S. McEwen, L. Ojha, C. M. Dundas et al., "Seasonal flows on warm Martian slopes," *Science*, vol. 333, no. 6043, pp. 740–743, 2011.

[17] J. D. Rummel, D. W. Beaty, M. A. Jones et al., "A new analysis of Mars "special regions": findings of the second MEPAG Special Regions Science Analysis Group (SR-SAG2)," *Astrobiology*, vol. 14, no. 11, pp. 887–968, 2014.

[18] J. R. Michalski, J. Cuadros, P. B. Niles, J. Parnell, A. D. Rogers, and S. P. Wright, "Groundwater activity on Mars and implications for a deep biosphere," vol. 6, no. 2, pp. 133–138, 2013.

[19] A. Embry and B. Beauchamp, "Sverdrup Basin," in *Sedimentary Basins of the World*, A. D. Miall, Ed., pp. 451–471, Elsevier, 2008.

[20] Z. Chen, K. G. Osadetz, A. F. Embry, H. Gao, and P. K. Hannigan, "Petroleum potential in western Sverdrup Basin, Canadian Arctic Archipelago," *Bulletin of Canadian Petroleum Geology*, vol. 48, no. 4, pp. 323–338, 2000.

[21] S. F. Jones, H. Wielens, M. C. Williamson, and M. Zentilli, "Impact of magmatism on petroleum systems in the Sverdrup Basin, Canadian Arctic Islands, Nunavut: a numerical modelling study," *Journal of Petroleum Geology*, vol. 30, no. 3, pp. 237–256, 2007.

[22] E. T. Tozer, *Mesozoic and Tertiary Stratigraphy, Western Ellesmere Island and Axel Heiberg Island, District of Franklin (Preliminary Account)*, Department of Mines and Technical Surveys, 1963.

[23] R. Thorsteinsson and E. T. Tozer, *Geology western Queen Elizabeth Islands, district of Franklin*, Geological survey of Canada, 1964, Map 1142A, scale 1:506,880.

[24] P. E. Fricker, *Geology of the Expedition Area: Western Central Axel Heiberg Island; Canadian Arctic Archipelago; Jacobsen-McGill Arctic Research Expedition 1959–1962*, McGill University, 1963.

[25] E. W. Hoen, *The Anhydrite Diapirs and Structure of Central Western Axel Heiberg Island: Canadian Arctic Archipelago, [M.S. thesis]*, McGill University, Montreal, Canada, 1962.

[26] E. W. Hoen, *The Anhydrite Diapirs of Central Western Axel Heiberg Island. Jacobsen-McGill Arctic Research Expedition 1959-1962 Research Reports, Geology, No. 2*, McGill University, Montreal, 1964.

[27] J. C. Harrison and M. P. Jackson, "Geology, Strand fiord-expedition fiord area, western Axel Heiberg Island, Nunavut," in *Geological survey of Canada, Map 2157A, scale 1:100 000*, Geological Survey of Canada, Ottawa, Canada, 2010.

[28] M. Villeneuve and M. C. Williamson, "40Ar-39Ar dating of mafic magmatism from the Sverdrup Basin Magmatic Province," in *Proceedings of the Fourth International Conference on Arctic Margins. Dartmouth, Nova Scotia, Canada 2003*, pp. 206–216, Anchorage, Alaska, 2006.

[29] P. Budkewitsch, W. Pollard, and M. Zentilli, *Youngest Hills in Axel Heiberg Island, Canadian Arctic Archipelago: Are the Salt Domes Rising?*, Geological Association of Canada Meeting, Ottawa, Canada, 2011.

[30] J. T. van Berkel, W. M. Schwerdtner, and J. G. Torrance, "Wall-and-basin structure: an intriguing tectonic prototype in the central Sverdrup Basin, Canadian Arctic Archipelago," *Bulletin of Canadian Petroleum Geology*, vol. 32, no. 4, pp. 343–358, 1984.

[31] W. M. Schwerdtner and M. Van Kranendonk, "Structure of Stolz Diapir – a well-exposed salt dome on Axel Heiberg Island, Canadian Arctic Archipelago," *Bulletin of Canadian Petroleum Geology*, vol. 32, no. 2, pp. 237–241, 1984.

[32] W. W. Nassichuk and G. R. Davies, "Biostratigraphy and sedimentology of the Otto Fiord Foration – a major Mississippian-Pennsylvanian evaporite unit of subaqueous origin in the Canadian Arctic Archipelago," *Geological Survey of Canada*, vol. 286, article 1087, 1980.

[33] L. I. Thomson and L. Copland, "White Glacier 2014, Axel Heiberg Island, Nunavut: mapped using structure from motion methods," *Journal of Maps*, vol. 12, no. 5, pp. 1063–1071, 2016.

[34] L. I. Thomson, M. Zempf, L. Copland, G. Cogley, and M. Ecclestone, "Comparison of geodetic and glaciological mass budgets for White Glacier, Axel Heiberg Island, Canada," *Journal of Glaciology*, vol. 63, no. 237, pp. 55–66, 2016.

[35] B. Lafuente, R. T. Downs, H. Yang, and N. Stone, "The power of databases: the RRUFF project," in *Highlights in Mineralogical Crystallography*, T. Armbruster and R. M. Danisi, Eds., pp. 1–30, W. De Gruyter, Berlin, Germany, 2015.

[36] R. J. Bodnar and M. O. Vityk, "Interpretation of Microthermometric Data for H2O-NaCl Fluid Inclusions," in *Fluid Inclusions in Minerals: Methods and Application*, B. Vivo and M. L. Frezzotti, Eds., Pontignsno-Siena, 1994117130.

[37] T. Driesner and C. A. Heinrich, "The system H_2O–NaCl. Part I: correlation formulae for phase relations in temperature–pressure–composition space from 0 to 1000°C, 0 to 5000 bar, and 0 to 1 X_{NaCl}," *Geochimica et Cosmochimica Acta*, vol. 71, no. 20, pp. 4880–4901, 2007.

[38] T. Driesner, "The system H_2O–NaCl. Part II: correlations for molar volume, enthalpy, and isobaric heat capacity from 0 to 1000°C, 1 to 5000 bar, and 0 to 1 X_{NaCl}," *Geochimica et Cosmochimica Acta*, vol. 71, no. 20, pp. 4902–4919, 2007.

[39] D. Günther and C. A. Heinrich, "Enhanced sensitivity in laser ablation-ICP mass spectrometry using helium-argon mixtures as aerosol carrier," *Journal of Analytical Atomic Spectrometry*, vol. 14, no. 9, pp. 1363–1368, 1999.

[40] D. Günther, R. Frischknecht, C. A. Heinrich, and H. J. Kahlert, "Capabilities of an argon fluoride 193 nm excimer laser for laser ablation inductively coupled plasma mass spectometry microanalysis of geological materials," *Journal of Analytical Atomic Spectrometry*, vol. 12, no. 9, pp. 939–944, 1997.

[41] T. Pettke, W. E. Halter, J. D. Webster, M. Aigner-Torres, and C. A. Heinrich, "Accurate quantification of melt inclusion chemistry by LA-ICPMS: a comparison with EMP and SIMS and advantages and possible limitations of these methods," *Lithos*, vol. 78, no. 4, pp. 333–361, 2004.

[42] M. Guillong, D. L. Meier, M. M. Allan, C. A. Heinrich, and B. W. Yardley, "Appendix A6: SILLS: a MATLAB-based program for the reduction of laser ablation ICP-MS data of homogeneous materials and inclusions," *Mineralogical Association of Canada Short Course Series*, vol. 40, pp. 328–333, 2008.

[43] A. M. Grist and M. Zentilli, "The thermal history of the Nares Strait, Kane Basin, and Smith Sound region in Canada and Greenland: constraints from apatite fission-track and (U Th Sm)/He dating," *Canadian Journal of Earth Sciences*, vol. 42, no. 9, pp. 1547–1569, 2005.

[44] G. Wagner and P. Van den Haute, *Fission Track Dating*, Kluwer Academic Publishers, Dordrecht, 1992, reprinted by Ferdinand Enke Verlag Thc Netherlands.

[45] C. E. Ravenhurst and R. A. Donelick, "Fission track thermochronology," in *Short Course Handbook on Low Temperature Thermochronology*, M. Zentilli and P. H. Reynolds, Eds., pp. 21–42, Mineralogical Association of Canada, Wolfville, Nova Scotia, Canada, 1992.

[46] K. Gallagher, R. Brown, and C. Johnson, "Fission track analysis and its applications to geological problems," *Annual Review of Earth and Planetary Sciences*, vol. 26, no. 1, pp. 519–572, 1998.

[47] A. J. Gleadow and R. W. Brown, "Fission-track thermochronology and the long-term denudational response to tectonics," in *Geomorphology and global tectonics*, M. J.

Summerfield, Ed., pp. 57–75, Wiley, New York, NY, USA, 2000.

[48] G. M. Laslett, P. F. Green, I. R. Duddy, and A. J. W. Gleadow, "Thermal annealing of fission tracks in apatite 2. A quantitative analysis," *Chemical Geology: Isotope Geoscience Section*, vol. 65, no. 1, pp. 1–13, 1987.

[49] P. Vrolijk, R. A. Donelick, J. Queng, and M. Cloos, "Testing models of fission track annealing in apatite in a simple thermal setting: site 800, leg 129," in *Proceedings of the Ocean Drilling Program, Scientific Results*, vol. 129, pp. 169–176, Ocean Drilling Program College Station, TX, USA, 1992.

[50] D. T. Andersen, W. H. Pollard, and C. P. McKay, "The perennial springs of Axel Heiberg Island as an analogue for groundwater discharge on Mars," in *9th International Conference on Permafrost*, vol. 2, pp. 2140–2145, Fairbanks, Alaska, 2008.

[51] W. H. Pollard, "Icing processes associated with High Arctic perennial springs, Axel Heiberg Island, Nunavut, Canada," *Permafrost and Periglacial Processes*, vol. 16, no. 1, pp. 51–68, 2005.

[52] S. E. Grasby, C. C. Allen, T. G. Longazo, J. T. Lisle, D. W. Griffin, and B. Beauchamp, "Supraglacial sulfur springs and associated biological activity in the Canadian High Arctic—signs of life beneath the ice," *Astrobiology*, vol. 3, no. 3, pp. 583–596, 2003.

[53] S. E. Grasby, B. C. Proemse, and B. Beauchamp, "Deep groundwater circulation through the High Arctic cryosphere forms Mars-like gullies," *Geology*, vol. 42, no. 8, pp. 651–654, 2014.

[54] A. E. Taylor and A. S. Judge, *Canadian Geothermal Data Collection-Northern Wells 1975*, Energy MaRC, Earth Physics Branch, Ottawa, 1978.

[55] C. R. Omelon, W. H. Pollard, and D. T. Andersen, "A geochemical evaluation of perennial spring activity and associated mineral precipitates at Expedition Fjord, Axel Heiberg Island, Canadian High Arctic," *Applied Geochemistry*, vol. 21, no. 1, pp. 1–15, 2006.

[56] C. R. Omelon, W. H. Pollard, and G. M. Marion, "Seasonal formation of ikaite ($CaCO_3{\cdot}6H_2O$) in saline spring discharge at Expedition Fiord, Canadian High Arctic: assessing conditional constraints for natural crystal growth," *Geochimica et Cosmochimica Acta*, vol. 65, no. 9, pp. 1429–1437, 2001.

[57] M. M. Battler, G. R. Osinski, and N. R. Banerjee, "Mineralogy of saline perennial cold springs on Axel Heiberg Island, Nunavut, Canada and implications for spring deposits on Mars," *Icarus*, vol. 224, no. 2, pp. 364–381, 2013.

[58] S. E. Grasby, "Naturally precipitating vaterite (μ-CaCO3) spheres - unusual carbonates formed in an extreme environment," *Geochimica et Cosmochimica Acta*, vol. 67, no. 9, pp. 1659–1666, 2003.

[59] W. H. Pollard and V. Everdingen, "R.O. 1992. Formation of seasonal ice bodies," *Periglacial Geomorphology, Proceedings of the 22nd Annual Binghamton Symposium in Geomorphology*, pp. 281–304, John Wiley & Sons, Chichester, UK.

[60] C.-Y. Lay, N. C. Mykytczuk, T. D. Niederberger, C. Martineau, C. W. Greer, and L. G. Whyte, "Microbial diversity and activity in hypersaline high Arctic spring channels," *Extremophiles*, vol. 16, no. 2, pp. 177–191, 2012.

[61] C.-Y. Lay, N. C. S. Mykytczuk, É. Yergeau, G. Lamarche-Gagnon, C. W. Greer, and L. G. Whyte, "Defining the functional potential and active community members of a sediment microbial community in a high-Arctic hypersaline subzero spring," *Applied and Environmental Microbiology*, vol. 79, no. 12, pp. 3637–3648, 2013.

[62] T. D. Niederberger, N. N. Perreault, J. R. Lawrence et al., "Novel sulfur-oxidizing streamers thriving in perennial cold saline springs of the Canadian high Arctic," *Environmental Microbiology*, vol. 11, no. 3, pp. 616–629, 2009.

[63] T. D. Niederberger, N. N. Perreault, S. Tille et al., "Microbial characterization of a subzero, hypersaline methane seep in the Canadian High Arctic," *The ISME Journal*, vol. 4, no. 10, pp. 1326–1339, 2010.

[64] N. N. Perreault, D. T. Andersen, W. H. Pollard, C. W. Greer, and L. G. Whyte, "Characterization of the prokaryotic diversity in cold saline perennial springs of the Canadian High Arctic," *Applied and Environmental Microbiology*, vol. 73, no. 5, pp. 1532–1543, 2007.

[65] N. N. Perreault, C. W. Greer, D. T. Andersen et al., "Heterotrophic and autotrophic microbial populations in cold perennial springs of the high Arctic," *Applied and Environmental Microbiology*, vol. 74, no. 22, pp. 6898–6907, 2008.

[66] D. T. Andersen, C. P. McKay, W. H. Pollard, and J. Heldmann, "Correction to "Cold springs in permafrost on Earth and Mars"," *Journal of Geophysical Research*, vol. 110, no. E4, article E04007, 2005.

[67] M. R. Hudec and M. P. Jackson, "Interaction between spreading salt canopies and their peripheral thrust systems," *Journal of Structural Geology*, vol. 31, no. 10, pp. 1114–1129, 2009.

[68] T. E. Hearon, M. G. Rowan, T. F. Lawton, P. T. Hannah, and K. A. Giles, "Geology and tectonics of Neoproterozoic salt diapirs and salt sheets in the eastern Willouran Ranges, South Australia," *Basin Research*, vol. 27, no. 2, pp. 183–207, 2015.

[69] J. K. Warren, "Salt usually seals, but sometimes leaks: implications for mine and cavern stabilities in the short and long term," *Earth-Science Reviews*, vol. 165, pp. 302–341, 2017.

[70] T. Pichler and J. Veizer, "The precipitation of aragonite from shallow water hydrothermal fluids in a coral reef, Tutum Bay, Ambitle Island, Papua New Guinea," *Chemical Geology*, vol. 207, no. 1-2, pp. 31–45, 2004.

[71] J. B. Murowchick, "Marcasite inversion and the petrographic determination of pyrite ancestry," *Economic Geology*, vol. 87, no. 4, pp. 1141–1152, 1992.

[72] P. R. L. Browne, "Aragonite deposited from Broadlands geothermal drillhole water," *New Zealand Journal of Geology and Geophysics*, vol. 16, no. 4, pp. 927–933, 1973.

[73] L. A. Casella, E. Griesshaber, X. Yin et al., "Experimental diagenesis: insights into aragonite to calcite transformation of Arctica islandica shells by hydrothermal treatment," *Biogeosciences*, vol. 14, no. 6, pp. 1461–1492, 2017.

[74] F. Ghazban, H. P. Schwarcz, and D. C. Ford, "Carbon and sulfur isotope evidence for in situ reduction of sulfate, Nanisivik lead-zinc deposits, Northwest Territories, Baffin Island, Canada," *Economic Geology*, vol. 85, no. 2, pp. 360–375, 1990.

[75] M. M. Savard, G. Chi, T. Sami, A. E. Williams-Jones, and K. Leigh, "Fluid inclusion and carbon, oxygen, and strontium isotope study of the Polaris Mississippi Valley-type Zn–Pb deposit, Canadian Arctic Archipelago: implications for ore genesis," *Mineralium Deposita*, vol. 35, pp. 495–510, 2000.

[76] G. E. Claypool, W. T. Holser, I. R. Kaplan, H. Sakai, and I. Zak, "The age curves of sulfur and oxygen isotopes in marine sulfate and their mutual interpretation," *Chemical Geology*, vol. 28, pp. 199–260, 1980.

[77] H. Ohmoto and R. O. Rye, "Isotopes of sulfur and carbon," *Geochemistry of Hydrothermal Ore Deposits*, H. L. Barnes, Ed., pp. 509–567, 1979.

[78] P. W. Reiners, T. A. Ehlers, and P. K. Zeitler, "Past, present, and future of thermochronology," *Reviews in Mineralogy and Geochemistry*, vol. 58, no. 1, pp. 1–18, 2005.

[79] J. C. Harrison, U. Mayr, D. H. McNeil et al., "Correlation of Cenozoic sequences of the Canadian *Arctic* region and Greenland; implications for the tectonic history of northern North America," *Bulletin of Canadian Petroleum Geology*, vol. 47, no. 3, pp. 223–254, 1999.

[80] W. R. Roest and S. P. Srivastava, "Sea-floor spreading in the Labrador Sea: a new reconstruction," *Geology*, vol. 17, no. 11, pp. 1000–1003, 1989.

[81] R. Buckley, A. M. Grist, and M. Zentilli, *Application of the (U-Th-Sm)/He in Apatite: Assessing the Paleothermal Effect of Salt Structures on Sverdrup Basin Rocks*, vol. 45, Atlantic Geology, Axel Heiberg Island, Nunavut, 2009.

[82] D. I. Issler, *An Inverse Model for Extracting Thermal Histories from Apatite Fission Track Data: Instructions and Software for the Windows 95 Environment*, Geological Survey of Canada, 1996, Open File Report, 2325.

[83] S. D. Willett, "Inverse modeling of annealing of fission tracks in apatite; 1, a controlled random search method," *American Journal of Science*, vol. 297, no. 10, pp. 939–969, 1997.

[84] A. M. Grist and M. Zentilli, "Preliminary apatite fission track thermal history modelling of the Nares region of eastern Ellesmere Island and northwestern Greenland," *Polarforschung*, vol. 74, no. 1–3, pp. 113–127, 2006.

[85] J. W. Hedenquist, E. Izaw, A. Arribas, and N. C. White, *Epithermal Gold Deposits: Styles, Characteristics, and Exploration*, Society of Resource Geology, Japan, Tokyo, 1996, Special publication no. 1.

[86] M. H. Reed, "Hydrothermal alteration and its relationship to ore fluid composition," in *Geochemistry of Hydrothermal Ore Deposits*, H. L. Barnes, Ed., pp. 303–366, Wiley, New York, NY, USA, 1997.

[87] H. Schneiderhöhn, "Chalkographische untersuchung des mansfelder kupferschiefers," *Neues Jahrbuch für Mineralogie, Geologie und Paläontologie*, vol. 47, pp. 1–38, 1923.

[88] N. S. Wilson, M. Zentilli, and B. Spiro, "A sulfur, carbon, oxygen, and strontium isotope study of the volcanic-hosted El Soldado manto-type copper deposit, Chile: the essential role of bacteria and petroleum," *Economic Geology*, vol. 98, no. 1, pp. 163–174, 2003.

[89] Z. Lin, X. Sun, J. Peckmann et al., "How sulfate-driven anaerobic oxidation of methane affects the sulfur isotopic composition of pyrite: a SIMS study from the South China Sea," *Chemical Geology*, vol. 440, pp. 26–41, 2016.

[90] Z. Sawlowicz, "Pyrite framboids and their development: a new conceptual mechanism," *Geologische Rundschau*, vol. 82, no. 1, pp. 148–156, 1993.

[91] R. T. Wilkin and H. L. Barnes, "Pyrite formation by reactions of iron monosulfides with dissolved inorganic and organic sulfur species," *Geochimica et Cosmochimica Acta*, vol. 60, no. 21, pp. 4167–4179, 1996.

[92] L. A. Vietti, J. V. Bailey, D. L. Fox, and R. R. Rogers, "Rapid formation of framboidal sulfides on bone surfaces from a simulated marine carcass fall," *PALAIOS*, vol. 30, no. 4, pp. 327–334, 2015.

[93] M. Farrand, "Framboidal sulphides precipitated synthetically," *Mineralium Deposita*, vol. 5, no. 3, pp. 237–247, 1970.

[94] P. Ramdohr, *The Ore Minerals and Their Intergrowths*, Pergamon Press Ltd., Oxford, England, 2nd edition, 1980.

[95] W. Shen, Y. Lin, L. Xu, J. Li, Y. Wu, and Y. Sun, "Pyrite framboids in the Permian–Triassic boundary section at Meishan, China: evidence for dysoxic deposition," *Palaeogeography, Palaeoclimatology, Palaeoecology*, vol. 253, no. 3-4, pp. 323–331, 2007.

[96] R. L. Folk, "Nannobacteria and the formation of framboidal pyrite: textural evidence," *Journal of Earth System Science*, vol. 114, no. 3, pp. 369–374, 2008.

[97] B. Cavalazzi, R. Barbieri, S. L. Cady et al., "Iron-framboids in the hydrocarbon-related Middle Devonian Hollard Mound of the Anti-Atlas mountain range in Morocco: Evidence of potential microbial biosignatures," *Sedimentary Geology*, vol. 263-264, pp. 183–193, 2012.

[98] J. R. Craig, F. M. Vokes, and T. N. Solberg, "Pyrite: physical and chemical textures," *Mineralium Deposita*, vol. 34, no. 1, pp. 82–101, 1998.

[99] G. Kullerud, "Sulfide studies," in *Researches in Geochemistry*, P. H. Adleson, Ed., pp. 286–321, Wiley, New York, NY, USA, 2 edition, 1967.

[100] F. M. Vokes, "The metamorphism of pyrite and pyritic ores: an overview," *Mineralogical Magazine*, vol. 57, no. 386, pp. 3–18, 1993.

[101] L. Fontboté and G. C. Amstutz, "Facies and sequence analysis of diagenetic crystallization rhythmites in strata-bound Pb-Zn-(Ba-F-) deposits in the Triassic of Central and Southern Europe," in *Mineral Deposits of the Alps and of the Alpine Epoch in Europe*, Springer, Berlin, Heidelberg, 1983.

[102] U. Kelka, M. Veveakis, D. Koehn, and N. Beaudoin, "Zebra rocks: compaction waves create ore deposits," *Scientific Reports*, vol. 7, no. 1, article 14260, 2017.

[103] M. W. Wallace, R. A. Both, S. M. Ruano, P. Fenoll Hach-Ali, and T. Lees, "Zebra textures from carbonate-hosted sulfide deposits; sheet cavity networks produced by fracture and solution enlargement," *Economic Geology*, vol. 89, no. 5, pp. 1183–1191, 1994.

[104] D. C. Arne and S. A. Kissin, "The significance of "diagenetic crystallization rhythmites" at the Nanisivik Pb-Zn-Ag deposit, Baffin Island, Canada," *Mineralium Deposita*, vol. 24, no. 3, pp. 230–232, 1989.

[105] D. C. Arne, L. W. Curtis, and S. A. Kissin, "Internal zonation in a carbonate-hosted Zn-Pb-Ag deposit, Nanisivik, Baffin Island. Canada," *Economic Geology*, vol. 86, no. 4, pp. 699–717, 1991.

[106] V. Badoux, R. Moritz, and L. Fontboté, "The Mississippi Valley-type Zn-Pb deposit of San Vicente, Central Peru: an Andean syntectonic deposit," in *Mineral Deposits at the Beginning of the 21st Century, Proceedings of the 6th Biennial SGA Meeting, Krakow, Poland*, pp. 191–195, Balkema Rotterdam, August 2001.

[107] M. King Hubbert and W. W. Rubey, "Role of fluid pressure in mechanics of overthrust faulting: I. mechanics of fluid-filled porous solids and its application to overthrust faulting," *Geological Society of America Bulletin*, vol. 70, no. 2, pp. 115–166, 1959.

[108] W. J. Phillips, "Hydraulic fracturing and mineralization," *Journal of the Geological Society*, vol. 128, no. 4, pp. 337–359, 1972.

[109] D. T. Secor, "Role of fluid pressure in jointing," *American Journal of Science*, vol. 263, no. 8, pp. 633–646, 1965.

[110] J. G. Ramsay, "The crack–seal mechanism of rock deformation," *Nature*, vol. 284, no. 5752, pp. 135–139, 1980.

[111] L. M. Cathles and A. T. Smith, "Thermal constraints on the formation of Mississippi Valley-type lead-zinc deposits and their implications for episodic basin dewatering and deposit genesis," *Economic Geology*, vol. 78, no. 5, pp. 983–1002, 1983.

[112] R. J. Ryan, A. M. Grist, and M. Zentilli, "The Paleozoic Maritimes Basin of Eastern Canada: metallogenetic implications of a fission track study," in *Short Course Handbook on Low Temperature Thermochronology*, M. Zentilli and P. H. Reynolds, Eds., pp. 141–155, Mineralogical Association of Canada, Wolfville, Nova Scotia, Canada, 1992.

[113] J. M. Sharp, "Energy and momentum transport model of the Ouachita basin and its possible impact on formation of economic mineral deposits," *Economic Geology*, vol. 73, no. 6, pp. 1057–1068, 1978.

[114] C. E. Ravenhurst and M. Zentilli, "A model for the evolution of hot (>200 C) overpressured brines under an evaporite seal: the Fundy/Magdalen Carboniferous Basin of Atlantic Canada and its associated Pb-Zn-Ba deposits," in *Sedimentary Basins and Basin Forming Mechanisms, Canadian Society of Petroleum Geologists*, T. Tankard and C. Beaumont, Eds., vol. 12, pp. 335–350, Memoir, 1987.

[115] W. S. Hallager, M. R. Ulrich, J. R. Kyle, P. E. Price, and W. A. Gose, "Evidence for episodic basin dewatering in salt-dome cap rocks," *Geology*, vol. 18, no. 8, pp. 716–719, 1990.

[116] M. W. Wallace and A. V. S. Hood, "Zebra textures in carbonate rocks: fractures produced by the force of crystallization during mineral replacement," *Sedimentary Geology*, vol. 368, pp. 58–67, 2018.

[117] D. W. Powers, R. H. Vreeland, and W. D. Rosenzweig, "Biogeology: how old are bacteria from the Permian age?," *Nature*, vol. 411, no. 6834, pp. 155-156, 2001.

[118] R. M. Holt and D. W. Powers, "Synsedimentary dissolution pipes and the isolation of ancient bacteria and cellulose," *GSA Bulletin*, vol. 123, no. 7-8, pp. 1513–1523, 2011.

[119] R. L. Beauheim and R. M. Roberts, "Hydrology and hydraulic properties of a bedded evaporite formation," *Journal of Hydrology*, vol. 259, no. 1–4, pp. 66–88, 2002.

[120] M. Zarei and E. Raeisi, "Karst development and hydrogeology of Konarsiah salt diapir, south of Iran," *Carbonates and Evaporites*, vol. 25, no. 3, pp. 217–229, 2010.

[121] E. Casas and T. K. Lowenstein, "Diagenesis of saline pan halite; comparison of petrographic features of modern, Quaternary and Permian halites," *Journal of sedimentary Research*, vol. 59, no. 5, pp. 724–739, 1989.

[122] C. E. Keen, "Salt diapirs and thermal maturity," *Bulletin of Canadian Petroleum Geology*, vol. 31, no. 2, pp. 101–108, 1983.

[123] D. G. Evans, J. A. Nunn, and J. S. Hanor, "Mechanisms driving groundwater flow near salt domes," *Geophysical Research Letters*, vol. 18, no. 5, pp. 927–930, 1991.

[124] J. A. Majorowicz and A. F. Embry, "Present heat flow and paleo-geothermal regime in the Canadian Arctic margin: analysis of industrial thermal data and coalification gradients," *Tectonophysics*, vol. 291, no. 1–4, pp. 141–159, 1998.

[125] J. G. Fyles, L. V. Hills, J. V. Matthews Jr. et al., "Ballast Brook and Beaufort formations (Late Tertiary) on northern Banks Island, Arctic Canada," *Quaternary International*, vol. 22-23, pp. 141–171, 1994.

[126] A. J. Hidy, J. C. Gosse, D. G. Froese, J. D. Bond, and D. H. Rood, "A latest Pliocene age for the earliest and most extensive Cordilleran Ice Sheet in northwestern Canada," *Quaternary Science Reviews*, vol. 61, pp. 77–84, 2013.

[127] N. Rybczynski, J. C. Gosse, C. R. Harington, R. A. Wogelius, A. J. Hidy, and M. Buckley, "Mid-Pliocene warm-period deposits in the High Arctic yield insight into camel evolution," *Nature Communications*, vol. 4, no. 1, article 1550, 2013.

[128] J. England, N. Atkinson, J. Bednarski, A. S. Dyke, D. A. Hodgson, and C. Ó. Cofaigh, "The Innuitian Ice Sheet: configuration, dynamics and chronology," *Quaternary Science Reviews*, vol. 25, no. 7-8, pp. 689–703, 2006.

[129] J. K. Staiger, J. C. Gosse, J. V. Johnson et al., "Quaternary relief generation by polythermal glacier ice," *Earth Surface Processes and Landforms*, vol. 30, no. 9, pp. 1145–1159, 2005.

[130] A. Margreth, A. S. Dyke, J. C. Gosse, and A. M. Telka, "Neoglacial ice expansion and late Holocene cold-based ice cap dynamics on Cumberland Peninsula, Baffin Island, Arctic Canada," *Quaternary Science Reviews*, vol. 91, pp. 242–256, 2014.

[131] A. Margreth, J. C. Gosse, and A. S. Dyke, "Quantification of subaerial and episodic subglacial erosion rates on high latitude upland plateaus: Cumberland Peninsula, Baffin Island, Arctic Canada," *Quaternary Science Reviews*, vol. 133, pp. 108–129, 2016.

[132] S. C. Stover, S. Ge, P. Weimer, and B. C. McBride, "The effects of salt evolution, structural development, and fault propagation on Late Mesozoic-Cenozoic oil migration: a two-dimensional fluid-flow study along a megaregional profile in the northern Gulf of Mexico Basin," *AAPG Bulletin*, vol. 85, no. 11, pp. 1945–1966, 2001.

[133] M. J. Osborne and R. E. Swarbrick, "Mechanisms for generating overpressure in sedimentary basins: A reevaluation," *AAPG bulletin*, vol. 81, no. 6, pp. 1023–1041, 1997.

[134] G. N. Oakey and R. Stephenson, "Crustal structure of the Innuitian region of Arctic Canada and Greenland from gravity modelling: implications for the Palaeogene Eurekan orogen," *Geophysical Journal International*, vol. 173, no. 3, pp. 1039–1063, 2008.

[135] J. B. Fein and J. V. Walther, "Calcite solubility in supercritical CO_2-H_2O fluids," *Geochimica et Cosmochimica Acta*, vol. 51, no. 6, pp. 1665–1673, 1987.

[136] J. R. Kyle and J. A. Saunders, *Metallic deposits in the Gulf Coast Basin of southern North America: Diverse mineralization styles in a young sedimentary basin*, Society and Economy Geologists, Littleton, CO, USA, Special Publication #4, 1996.

[137] J. R. Kyle and J. A. Saunders, "Metallic deposits in the Gulf Coast Basin of southern North America: Diverse mineralization styles in a young sedimentary basin," in *Proceedings, Society and Economy Geol., Intern. Conf. on Carbonate-hosted Lead-Zinc Deposits*, pp. 218–229, 1996.

[138] M.-C. Williamson, Ed., *Environmental and Economic Significance of Gossans*, Geological Survey of Canada, 2015, Open File 7718.

[139] R. F. Galbraith and G. M. Laslett, "Statistical models for mixed fission track ages," *Nuclear Tracks and Radiation Measurements*, vol. 21, no. 4, pp. 459–470, 1993.

[140] J. R. O'Neil, R. N. Clayton, and T. K. Mayeda, "Oxygen isotope fractionation in divalent metal carbonates," *The Journal of Chemical Physics*, vol. 51, no. 12, pp. 5547–5558, 1969.

[141] Y. F. Zheng, "Oxygen isotope fractionation in carbonate and sulfate minerals," *Geochemical Journal*, vol. 33, no. 2, pp. 109–126, 1999.

[142] R. N. Clayton, J. R. O'Neil, and T. K. Mayeda, "Oxygen isotope exchange between quartz and water," *Journal of Geophysical Research*, vol. 77, no. 17, pp. 3057–3067, 1972.